

# Structural insights into the activation of metabotropic glutamate receptors

Antoine Koehl<sup>1,10</sup>, Hongli Hu<sup>1,2,10</sup>, Dan Feng<sup>3,10</sup>, Bingfa Sun<sup>3</sup>, Yan Zhang<sup>1,2</sup>, Michael J. Robertson<sup>1,2</sup>, Matthew Chu<sup>3</sup>, Tong Sun Kobilka<sup>2,3</sup>, Toon Laeremans<sup>4,5</sup>, Jan Steyaert<sup>4,5</sup>, Jeffrey Tarrasch<sup>6</sup>, Somnath Dutta<sup>6,9</sup>, Rasmus Fonseca<sup>1,2,7</sup>, William I. Weis<sup>1,2</sup>, Jesper M. Mathiesen<sup>8\*</sup>, Georgios Skiniotis<sup>1,2\*</sup> & Brian K. Kobilka<sup>2,3\*</sup>

**Metabotropic glutamate receptors are family C G-protein-coupled receptors. They form obligate dimers and possess extracellular ligand-binding Venus flytrap domains, which are linked by cysteine-rich domains to their 7-transmembrane domains. Spectroscopic studies show that signalling is a dynamic process, in which large-scale conformational changes underlie the transmission of signals from the extracellular Venus flytraps to the G protein-coupling domains—the 7-transmembrane domains—in the membrane. Here, using a combination of X-ray crystallography, cryo-electron microscopy and signalling studies, we present a structural framework for the activation mechanism of metabotropic glutamate receptor subtype 5. Our results show that agonist binding at the Venus flytraps leads to a compaction of the intersubunit dimer interface, thereby bringing the cysteine-rich domains into close proximity. Interactions between the cysteine-rich domains and the second extracellular loops of the receptor enable the rigid-body repositioning of the 7-transmembrane domains, which come into contact with each other to initiate signalling.**

Metabotropic glutamate receptors (mGlu) are G-protein-coupled receptors (GPCRs) that are activated by the excitatory neurotransmitter L-glutamate<sup>1,2</sup>. Family C receptors are unusual in that, as well as the GPCR-defining 7-transmembrane (7TM) domain, they possess relatively large amino-terminal extracellular domains (ECDs) that form obligate dimers and contain the orthosteric ligand-binding sites. In the mGlu subfamily, the ECD is composed of a conserved, ligand-binding Venus flytrap (VFT) domain and a cysteine-rich domain (CRD). The VFT is connected to the 7TM domain by the CRD, which provides a semi-rigid linker between the ligand-binding and the 7TM (signalling) domains<sup>2</sup>. Previous structural work on VFTs in isolation has shown that agonist binding leads to two major structural changes in the conformation of the dimer. The first is a closure of the two VFT lobes<sup>3</sup>. Signalling studies in live cells have suggested that VFT closure is essential for activation—closure of one lobe is sufficient for signalling, whereas closure of both lobes is necessary for full efficacy<sup>4</sup>. The second conformational change involves an intersubunit reorientation that brings the CRDs of the adjacent VFTs into close proximity to each other<sup>3</sup> (Fig. 1a). Fluorescence resonance energy transfer studies of full-length receptors in live cells have shown that activation probably depends on sequential inter- and intrasubunit conformational changes<sup>5</sup>.

The 7TM domain of mGlu receptors is the binding site of various non-endogenous allosteric ligands that can modulate signalling either alone or in conjunction with orthosteric ligands, thereby acting as positive allosteric modulators (PAMs) or negative allosteric modulators (NAMs). Crystal structures of the mGlu1<sup>6</sup> and mGlu5 7TM<sup>7–9</sup> domains show that the allosteric ligand-binding pockets largely overlap with those of orthosteric ligands in family A GPCRs<sup>10</sup>. Isolated 7TM domains also function similarly to rhodopsin-like GPCRs, with PAMs acting similarly to agonists at family A receptors<sup>11</sup>. It is noteworthy that many PAMs that are normally silent in full-length receptors act as full

agonists at isolated 7TM domains<sup>12</sup>, which suggests that the conformation of the extracellular domains of the mGlu receptor is a critical regulator of activation and signalling. To understand how agonist binding at the VFT is relayed over 120 Å to the intracellular G-protein-coupling region of the 7TM domain, we used a combination of cryo-electron microscopy (cryo-EM), X-ray crystallography and biochemical assays to obtain structures of the mGlu5 dimer in the inactive and active states.

## Structures of active-conformation-stabilizing ligands

For structural studies, we sought to complement orthosteric and allosteric small-molecule ligands with a nanobody—a single-chain camelid antibody—that could further stabilize the receptor in one conformation<sup>13</sup>. We therefore immunized a llama with full-length mGlu5, and after an initial screen for receptor binding and function we selected one nanobody, termed Nb43, on the basis of its ability to potentiate orthosteric agonist binding. Whereas the orthosteric endogenous agonist L-glutamate displaces the orthosteric analogue [<sup>3</sup>H]L-quisqualic acid from its orthosteric binding site, both Nb43 and the 7TM-domain-binding PAM-agonist 3-cyano-N-1,3-diphenyl-1*H*-pyrazol-5-yl) benzamide (CDPPB) exhibited positive binding cooperativity with [<sup>3</sup>H]L-quisqualic acid (Fig. 1b, Supplementary Table 1). Despite previous conflicting reports<sup>14–16</sup>, CDPPB was found to increase the affinity and the maximal binding capacity of [<sup>3</sup>H]L-quisqualic acid, which suggests the existence of a tight structural coupling between the VFT and 7TM domains (Supplementary Fig. 1, Supplementary Table 2). Functionally, L-glutamate and L-quisqualate induce G<sub>q</sub> coupling, which in turn leads to intracellular calcium release (Fig. 1c, Supplementary Table 3). During initial functional testing of Nb43 and CDPPB, both ligands seemed to potently activate mGlu5 (Fig. 1c). Because high receptor expression levels<sup>17</sup>—as well the presence of minute amounts of glutamate in the assay medium—are known confounders of these

<sup>1</sup>Department of Structural Biology, Stanford University School of Medicine, Stanford, CA, USA. <sup>2</sup>Department of Molecular and Cellular Physiology, Stanford University School of Medicine, Stanford, CA, USA. <sup>3</sup>ConfometRx, Santa Clara, CA, USA. <sup>4</sup>Structural Biology Brussels, Vrije Universiteit Brussel (VUB), Brussels, Belgium. <sup>5</sup>VIB-VUB Center for Structural Biology, VIB, Brussels, Belgium. <sup>6</sup>Life Sciences Institute and Department of Biological Chemistry, University of Michigan Medical School, Ann Arbor, MI, USA. <sup>7</sup>Biosciences Division, SLAC National Accelerator Laboratory, Stanford University, Stanford, CA, USA. <sup>8</sup>Department of Drug Design and Pharmacology, Faculty of Health and Medical Sciences, University of Copenhagen, Copenhagen, Denmark. <sup>9</sup>Present address: Molecular Biophysics Unit, Indian Institute of Science, Bangalore, India. <sup>10</sup>These authors contributed equally: Antoine Koehl, Hongli Hu, Dan Feng. \*e-mail: jmm@sund.ku.dk; yiorgo@stanford.edu; kobilka@stanford.edu

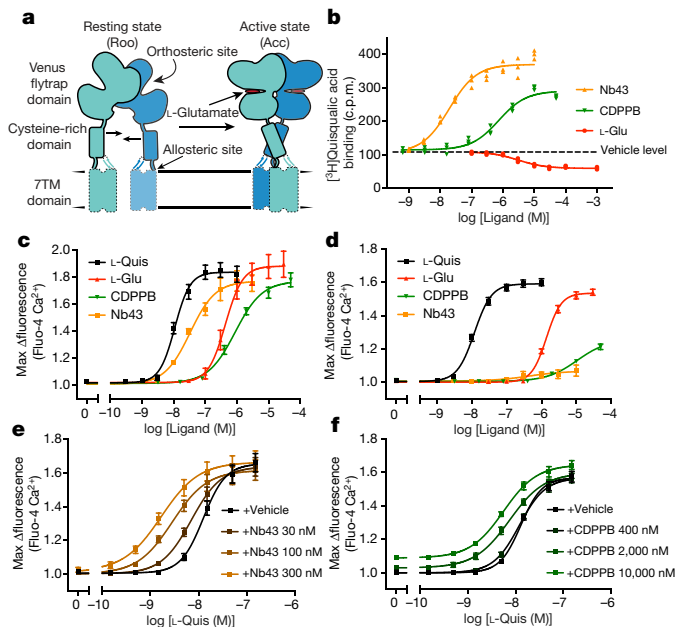


**Fig. 1 | mGlu5 activation through orthosteric and allosteric ligands.** **a**, Schematic of mGlu5 activation, with major domains labelled. ECDs are solidly outlined, whereas 7TM domains are indicated by a dashed line owing to previous uncertainty in their position. **b**, Nb43 and CDPPB show positive binding cooperativity with the radioligand [<sup>3</sup>H]L-quisqualate, whereas L-glutamate displaces the radioligand from the orthosteric binding site. **c–f**, In the absence of co-transfection of the neuronal EAAT3, Nb43 and CDPPB show high intrinsic activity at mGlu5, probably due to ambient cellular-released glutamate. **d**, Co-expression of EAAT3 completely removes the intrinsic activity of Nb43 and substantially reduces the intrinsic activity of CDPPB. **e**, **f**, Nb43 (**e**) and CDPPB (**f**) increase the potency and thereby show signalling cooperativity with L-quisqualate. For **b**, individual data points from one representative experiment performed in triplicate is shown of three independent experiments with similar results. For **c–f**, data represent mean  $\pm$  s.e.m. from four (**c**) or five (**d**, **e**, **f**) independent experiments.

assays<sup>18</sup>, we overexpressed the neuronal excitatory amino acid transporter 3 (EAAT3) together with lower levels of mGlu5 that are similar to those observed in cortical astrocytes<sup>16</sup> (Supplementary Table 5). Under these conditions, Nb43 had almost no intrinsic activity and that of CDPPB was considerably reduced (Fig. 1d). Nonetheless, Nb43 and CDPPB functionally potentiated each other (Supplementary Fig. 1) as well as L-quisqualate (Fig. 1e, f, Supplementary Table 3), which suggests that they act as PAMs to further stabilize an active signalling complex.

To understand the binding mode of Nb43 and its cooperativity with orthosteric agonists, we solved the X-ray structures of the amino-terminal domain of mGlu5 in complex with the nanobody both in the presence and in the absence of L-quisqualate (Fig. 2). Our construct extends through the CRD of mGlu5; however, in the apo state this region has weak electron density protruding diametrically opposite to the CRD of the second monomer, thereby assuming an orientation that is incompatible with a membrane-anchored receptor dimer (Extended Data Fig. 1a). Nb43 binds the apex of the VFT domain (Fig. 2a), with most contacts occurring between the complementarity determining regions 2 and 3 (CDR2 and CDR3) of the nanobody and two loops formed by residues 345–357 and residues 365–375 on mGlu5, respectively (Fig. 2a, b, Extended Data Fig. 1b, c). The binding interface of Nb43 is defined by two tryptophan residues (Trp107 and Trp110) that fold CDR3 against the core regions of the nanobody and orient it for binding within a groove at the apex of the VFT (Extended Data Fig. 1d). The majority of interactions between Nb43 and mGlu5 are polar (Fig. 2b) and involve residues that are poorly conserved among mGlu receptor subtypes (Extended Data Fig. 1c), which suggests that Nb43 would be a subtype-selective PAM of mGlu5. Overall, the

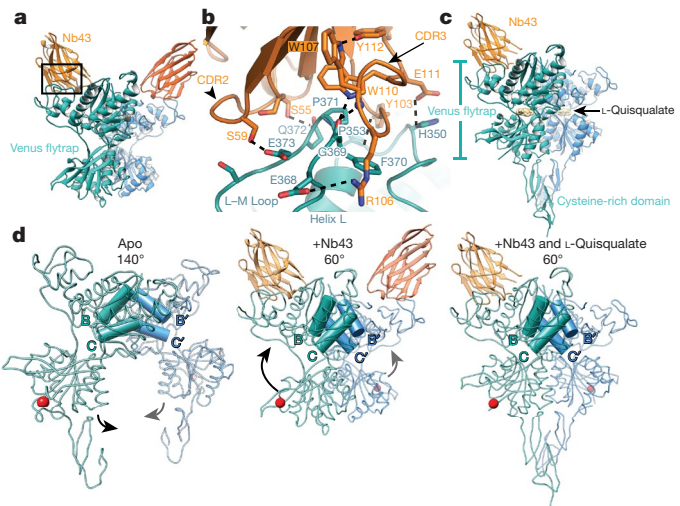


**Fig. 2 | X-ray structures of mGlu5 ECD in complex with Nb43.** **a**, Overall structure of the mGlu5 ECD in complex with Nb43. **b**, Nb43 binds the apex of the VFT through a series of polar interactions. **c**, The overall structure of the mGlu5 ECD with Nb43 and L-quisqualate is similar to that with only Nb43, but shows a pronounced intersubunit CRD interface. **d**, The activation process is highlighted by structures of the mGlu5 ECD alone (left), with Nb43 (middle) and with Nb43 and L-quisqualate (right). Both Nb43 and L-quisqualate lead to an intersubunit reorientation as measured by a reduced B–C helix angle. This brings the VFT bottom lobes together, as indicated by a red sphere at the C terminus of the VFT (Asp497).

architecture of this VFT dimer is that of an ‘Aoo’ (active open–open) form<sup>19</sup>, which has been observed very infrequently in crystal structures of antagonist-bound ECDs of mGlu1 (Protein Data Bank (PDB): 3SK9) and mGlu2 (PDB: 5KZN)<sup>20</sup>. The Aoo form is characterized by the close proximity of the VFT bottom lobes despite the flytraps being open (Fig. 2d, middle).

We also solved the crystal structure of the mGlu5 extracellular domain in the presence of Nb43 and L-quisqualate at a resolution of 3.75 Å. Although we do observe strong CRD density, our resolution limited us to mostly backbone modelling of this region (Extended Data Fig. 1e). We also modelled only one nanobody in the dimer, although we observe diffuse, positive density at the expected location of the second nanobody. Overall, this structure looks almost identical to that of the mGlu5 VFT in complex with glutamate (PDB: 3LMK) (root mean squared deviation, r.m.s.d., of 0.5 Å), and we observe the canonical agonist-bound ‘Acc’ (active closed–closed) VFT conformation (Fig. 2c) that, similar to the Aoo form presented above, is typified by a close proximity between VFT bottom lobes (Fig. 2c, d). Compared to the Nb43-apo structure, the binding of L-quisqualate not only leads to closure of the VFT lobe around the ligand but also results in the establishment of a defined intersubunit CRD interaction interface (Fig. 2c, d). This close apposition of the CRDs is consistent with observations that the introduction of intersubunit CRD crosslinks leads to constitutive activity in mGlu receptors<sup>21</sup>.

Despite extensive optimization, crystals of a full-length construct of mGlu5 bound to the F-MTEB analogue 3-fluoro-5-(2-(2-(fluoromethyl)thiazol-4-yl)ethynyl)benzonitrile<sup>22</sup> (FFMTEB), a potent and selective NAM, diffracted to only 4 Å resolution and lacked interpretable electron density in the transmembrane domain. Nonetheless, we were able to build and refine a model of the VFT and parts of the CRD domains (Fig. 2d, left) in their apo form. A comparison of this structure with that of the Nb43 complex and the complex with both Nb43 and L-quisqualate elucidates the structural transitions that underlie activation at the extracellular domain of mGlu5. Agonist binding reorients the dimer interface from the resting to the active state, as measured by a reduced B–C helix angle<sup>3</sup>, and leads to a conformation in which the VFT bottom lobes are located proximally to each other. The CRDs are

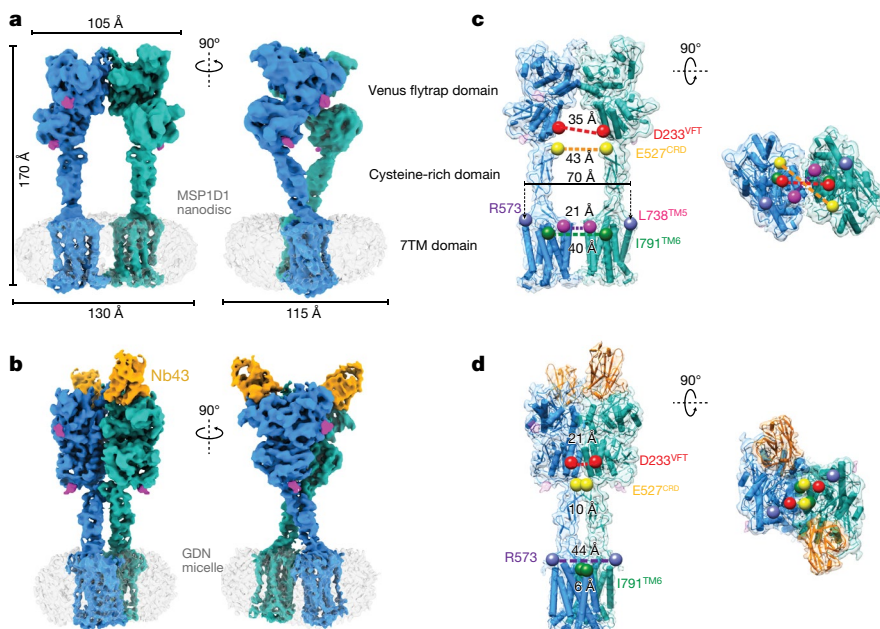


**Fig. 3 | Cryo-EM maps and models of full-length mGlu5.** **a, b**, Cryo-EM maps of full-length mGlu5 in the apo-VFT state (**a**) and the active state bound to Nb43 and L-quinalate (**b**). In **a** and **b**, the left panels show the same view of mGlu5 in the apo and active conformations, respectively; and the right panels show the view after a 90° rotation as indicated. **c, d**, Models of apo (**c**) and active (**d**) mGlu5 are shown viewed from the side (left) and top (right). Positions in the VFT (red), CRD (yellow), CRD/7TM interface (purple) and 7TM domain (green) show that the active state is characterized by smaller intersubunit distances. The TM5 position in the apo model (pink) shows that, at their closest point, the 7TM domains remain separated.

accordingly repositioned to relay this conformational change towards the membrane (Fig. 2d).

### Cryo-EM structures of full-length mGlu5

To better understand activation in the full-length mGlu5, we used cryo-EM to obtain structures of the receptor dimer in both the inactive and the active states (Extended Data Fig. 2b–f). Initial efforts to obtain the structure of detergent-reconstituted mGlu5 in the inactive (apo) state revealed a large population of receptors with split micelles that each contained one of the 7TM domains, which suggests that the inactive state is characterized by a lack of strong interactions between the transmembrane domains (Extended Data Fig. 2a). Given the possibility that the 7TM domain separation is a result of detergent solubilization, we reconstituted mGlu5 into nanodiscs and obtained a cryo-EM map of the full-length receptor at an overall resolution of 4.0 Å (Fig. 3a, Extended Data Figs. 2–4). This map enabled us to build a full-length apo-state model of mGlu5 including unambiguous placement of all transmembrane helices, aided in part by the availability of crystal structures of all components<sup>7,23</sup> (Extended Data Fig. 5a, b). The inactive conformation of mGlu5 involves a single interaction interface at the apex of the VFT domain (Fig. 3a, Extended Data Fig. 6, top). This interface, mostly formed by hydrophobic residues, is further stabilized by the conserved disulfide bond between the Cys129 residues of each subunit; however, this disulfide bond is not required for either dimer formation or signalling<sup>24</sup>. We note that the cryo-EM map lacks density for residues 123–135, and therefore we cannot confidently model the position of the disulfide. Although our crystal structure of apo mGlu5 only allowed for building of the ECD (as discussed above), its observed conformation is in the context of a full-length receptor that is restrained by its 7TM domains in detergent. It therefore enables a direct comparison with the cryo-EM structure, which includes density for all domains. Both structures show nearly identical ECD conformations, as evidenced by a backbone r.m.s.d. of 0.9 Å (Extended Data Fig. 7a), with the conformation of the CRDs indicating well-separated 7TM domains.

We prepared a stable, detergent-solubilized mGlu5 in the presence of L-quinalate, CDPPB and Nb43, enabling us to obtain a cryo-EM map of an active-state complex at a global resolution of 4.0 Å (Fig. 3b). The map shows well-resolved features in the VFT and the CRD domains (Extended Data Figs. 4, 5c–f) and, despite the lower local resolution in the transmembrane portion, it enables unambiguous placement of transmembrane helices (Fig. 3b, Extended Data Figs. 4, 5g, h). The active state of mGlu5 is very compact, with interactions between subunits at each of the VFT, CRD and 7TM domains (Fig. 3b, Extended

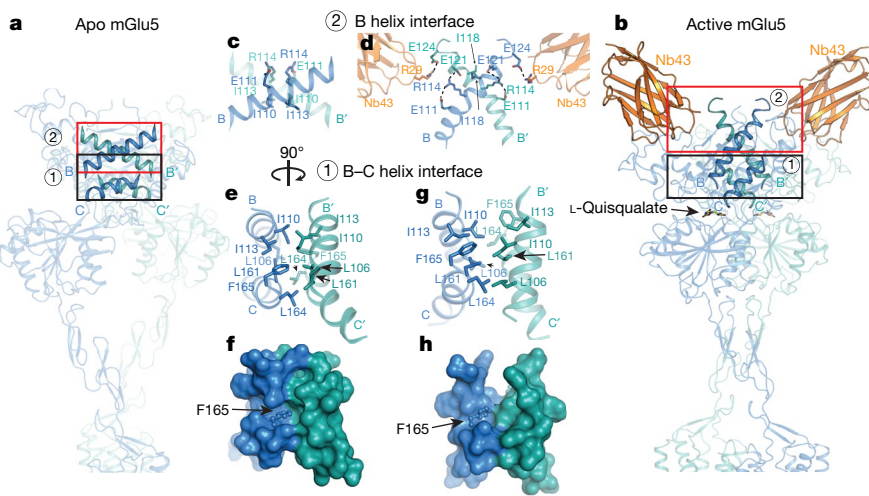
Data Fig. 6, bottom). This is further demonstrated by a substantially buried surface area of 2,160 Å<sup>2</sup> compared to 630 Å<sup>2</sup> in the inactive state (Extended Data Fig. 6).

### Activation leads to compaction of the mGlu5 dimer

The cryo-EM structures of full-length mGlu5 in active and inactive states complement our crystallographic observations of the ECDs, and explain how ligand binding at the ECD is relayed to the 7TM domain. Globally, agonist binding leads to a substantial compaction of the mGlu receptor dimer (Fig. 3c, d, Supplementary Video 1). In its apo state, the mGlu5 VFT adopts an ‘Roo’ (resting open–open) conformation with a bottom lobe separation of 35 Å at Asp233, whereas in the agonist-bound Acc conformation, this distance is reduced to 21 Å. In both states, the CRDs extend almost straight down from the C terminus of the VFT towards the membrane. In the inactive state, the average separation at Glu527 of the CRD is 43 Å, whereas this distance is reduced to 10 Å in the active state. The 7TM domains are completely separated in the inactive state; a backbone distance of 21 Å is observed between the TM5 helices of the two protomers, which are the most proximal transmembrane helix pair (Fig. 3c). In the active state the 7TM domains show a strong interaction along the TM6 helices, with a backbone separation distance of 6 Å at Ile791 (Fig. 3d).

The individual 7TM domains of both apo- and agonist-bound mGlu5 align well with each other and are almost identical in conformation to thermostabilized NAM-bound crystal structures<sup>7–9</sup> of the mGlu5 transmembrane domain in isolation (r.m.s.d. of 1.4 Å) (Extended Data Fig. 7c, d). Although the local resolution of the 7TM domains in both of our maps precludes unambiguous assignment of the state of the ligand at the allosteric site, the full agonist L-quinalate appears unable to stabilize an active conformation within the 7TM bundle. This observation is not entirely unexpected, as most family A receptors do not fully adopt their active conformation in the absence of intracellular stabilizers such as G proteins<sup>25,26</sup>. The structure of an active family C 7TM domain therefore remains unknown.

Agonist-induced structural changes are thought to be in part regulated by a hydrophobic patch of residues formed by the B and C helices at the apical surface of the VFT (Fig. 4a, b). Notably, this hydrophobic patch is the only interface that is conserved between apo and active mGlu5 (see above, Extended Data Fig. 6). Single-molecule fluorescence resonance energy transfer studies in mGlu2 showed that mutations that weaken this interface not only lead to increased glutamate affinity, but also to increased occupancy of the active conformation, even in the absence of agonists<sup>27</sup>. Our structures complement these results.



Compared to the tight interactions of the apo state (Fig. 4e, f), the active state shows a more open interface (Fig. 4g, h). Because the loops that immediately precede both the B and C helices contain residues that are important for ligand recognition, the binding of an agonist in the VFT may trigger relaxation of the B-C intersubunit interface, which releases its constraint upon activation. A further network of polar interactions at the apical surface of the B helices helps to stabilize the active conformation. Notably, Arg114 releases its interaction with Glu111 (Fig. 4c) of the complementary subunit to engage the more distal Glu121 (Fig. 4d), and thus helps to maintain the acute intersubunit B-helix angle that defines the active state. Unexpectedly, we also observed a potential interaction between Arg29 of Nb43 and Glu124 on the B helix of the protomer opposite to its major binding interface, which may provide a structural explanation for the allosteric properties of Nb43 (Fig. 4d). We note, however, that Nb43 alone cannot stabilize the active receptor conformation and the CRD interface. This interpretation is supported by cryo-EM analysis of full-length mGlu5 with bound Nb43 in the absence of an orthosteric ligand, which shows a dimer configuration that is very similar to the apo state (Extended Data Fig. 3b). Consistent with this finding, our molecular dynamics simulations show that Nb43 binding alone does not induce closure of the VFTs, but restricts them from opening to the extent of the fully inactive conformation (Extended Data Fig. 8).

**Fig. 4 | Structural changes at the VFT. a-h,** Comparison of intersubunit VFT interfaces in the apo (**a**) and active (**b**) states of mGlu5. The first interface is a hydrophobic patch between residues on the B and C helices (black boxes). In the apo form we observe a tight interface (**e, f**), whereas the active state is characterized by a more open interface (**g, h**). **f** and **h** show surface representations of **e** and **g**, respectively. The slipping of the B helices relative to each other leads to rearrangement of a polar interface around Arg114 (red boxes and **c, d**). Further stabilization may be provided by Nb43 (**d**).

## Activation of mGlu5 reorients the 7TM interface

Although dimeric associations between normally monomeric family A receptors have been observed in crystal structures, they show varied interaction interfaces and their physiological relevance is debated<sup>28-30</sup>. Previous work on mGlu1 and mGlu2 has led to contradicting models of the relative intersubunit transmembrane interface. Whereas the crystal structure of the mGlu1 7TM domain bound to the negative modulator 4-fluoro-N-(4-(6-(isopropylamino)pyrimidin-4-yl)thiazol-2-yl)-N-methylbenzamide (FITM) suggested a sterol-rich TM1 interface<sup>6</sup>, crosslinking studies of mGlu2 proposed an inactive state mediated by TM4 and TM5 that transitions to a TM6-driven interface in the presence of an agonist<sup>31</sup>.

Our structures revealed that, in addition to moving closer to each other, there is a 20° rotation of each 7TM upon activation (Fig. 5a–d, Extended Data Fig. 9a, b). Consequently, the TM1–TM1 distance decreases from around 70 Å in the inactive state to around 43 Å in the active state, as previously proposed<sup>31</sup> (Fig. 5c, d). More importantly, the propagation of structural changes leads to a TM6–TM6 interface that appears to be a hallmark of activation (Fig. 5d). This ‘active’ TM6 interface was confirmed by the introduction of a cysteine-mediated crosslink at the extracellular face of TM6 (I791<sup>6,56</sup>C after removal of the crosslink in the VFT(C129A)) (Extended Data Fig. 9c) (superscripts indicate generic GPCR numbering<sup>32</sup>). Surface expression levels of the

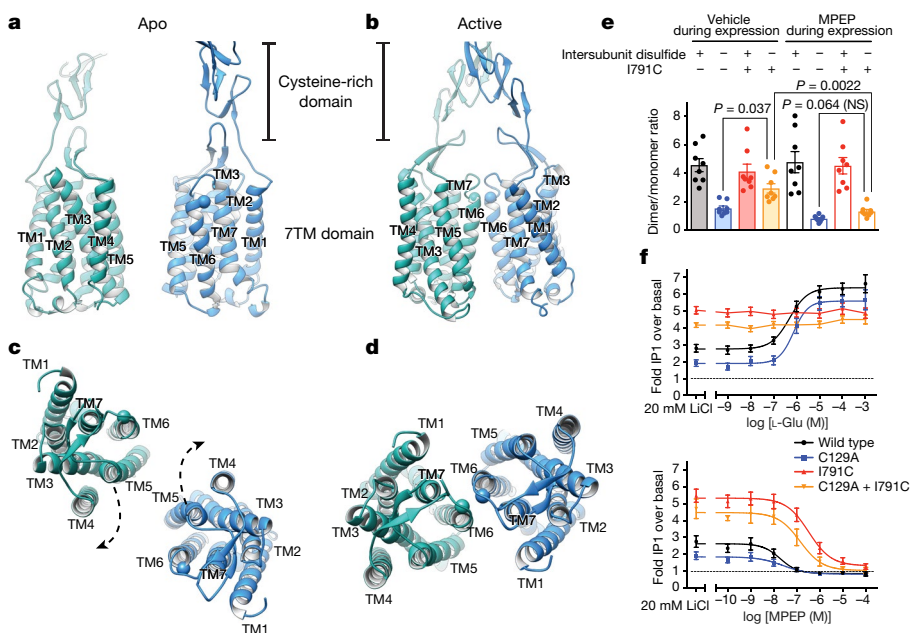


**Fig. 5 | Activation leads to a rearrangement of the 7TM interface.** **a–d**, Side (**a, b**) and top (**c, d**) views of apo (**a, c**) and active (**b, d**) mGlu5 CRD and 7TM domains. Both apo and active mGlu5 are shown in the same view after alignment to each other to enable direct comparison. The position of I791<sup>6,56</sup> is shown as a sphere for reference. **e**, Crosslinking of TM6 and subsequent re-establishment of the homodimer after removal of the crosslink in the VFTs by a C129A mutation is less efficient when the receptor is bound to a NAM (MPEP; yellow bars). **f**, A TM6 crosslinked mGlu5 is constitutively active (top) but responds to a 7TM negative modulator (bottom). Bars in **e** represent mean  $\pm$  s.e.m. from eight independent experiments. Statistics were performed using repeated measures one-way ANOVA followed by Tukey's multiple comparisons test and indicated *P* values were adjusted to account for multiple comparisons. Data in **f** represent mean  $\pm$  s.e.m. from five (top) and six (bottom) independent experiments performed in duplicate.

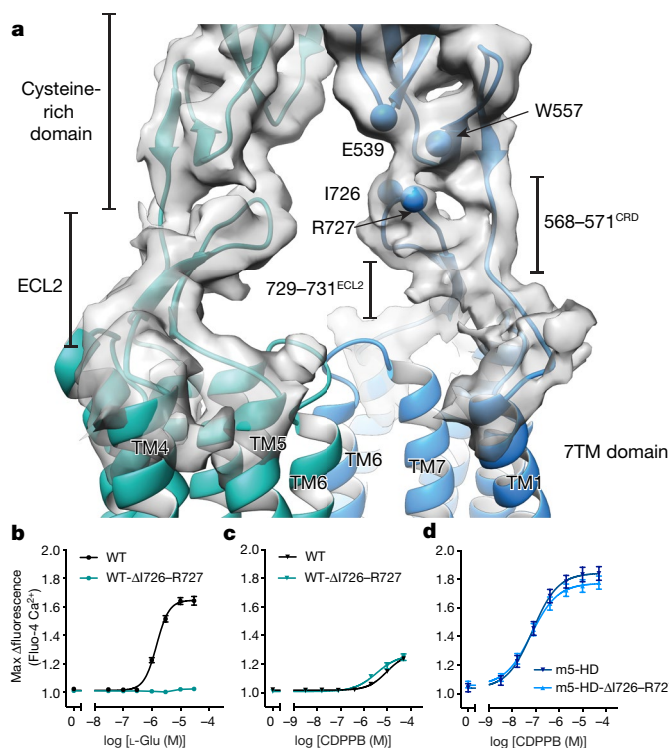


**Fig. 6 | ECL2 is necessary for activation by orthosteric agonists.** **a**, Model (teal and blue) and cryo-EM map (grey) showing interactions between the ECL2 of the 7TM domain and the CRD. Critical residues at this interface are shown as spheres at their  $C\alpha$  positions. **b–d**, Deletion of the distal loop residues in ECL2 leads to compromised signalling by the orthosteric agonist upon low expression of mGlu5 and co-transfection of EAAT3 (**b**) whereas the effect of the ago-PAM CDPPB is not compromised (**c**), probably reflecting disruption of the functional coupling of VFT with the 7TM domain. This deletion has no effect on signalling by the ago-PAM CDPPB at the 7TM domain alone (**d**). Data in **b–d** represent mean  $\pm$  s.e.m. from six independent experiments performed in duplicate or triplicate.

C129A, I791<sup>6,56</sup>C and C129A + I791<sup>6,56</sup>C mutants are comparable to those of the wild type (Supplementary Fig. 3). The C129A + I791<sup>6,56</sup>C mutant was found to spontaneously undergo dimer formation, but with higher efficiency in the absence of the NAM 2-methyl-6-(phenylethynyl)pyridine (MPEP) (Fig. 5e, Extended Data Fig. 9d). The TM6-crosslinked mGlu5 is constitutively active (Fig. 5f, top) and is not responsive to orthosteric agonists, a finding that was previously observed in an I<sup>6,56</sup>C TM6-locked mGlu2<sup>31</sup>. Notably, despite being locked in an active conformation, the I791C mutant receptor is still responsive to the 7TM NAM MPEP, which inhibited signalling in a dose-dependent manner (Fig. 5f, bottom) albeit with lower potency. The fact that a 7TM NAM is able to overcome the constitutive activity of the TM6-locked construct strongly suggests that the activation profile of mGlu receptors requires both inter- and intrasubunit conformational changes<sup>5</sup>.

### Propagation of orthosteric activation signals

Our cryo-EM structures of both active and inactive mGlu5 reveal an unexpected intrasubunit interaction between the CRD and extracellular loop (ECL2) of the 7TM domain (Fig. 6a). A first hint into the potential role of ECL2 in aiding signal transduction came from the crystal structure of the mGlu1 7TM domain<sup>6</sup>, which featured an extended ECL2 hairpin that projected outwards towards TM1 and the space in which the CRD was predicted to reside<sup>33</sup>. Notably, the conformation of ECL2 in our full-length structure is almost identical to that of the mGlu1 7TM domain. Despite the limited resolution of our maps, we can model two interaction interfaces using previous structural information as a guide. Interface 1 involves a short hydrophobic

interface between residues 729–731 of ECL2 and residues 568–571 at the CRD–TM1 boundary (Fig. 6a). Interface 2 encompasses residues 725–727 at the apical loop of the ECL2  $\beta$ -hairpin and a composite interface composed of residues Glu539 and Trp557 of the CRD (Fig. 6a). In particular, the chemistry and proximity of Arg727 in ECL2 enables it to potentially form interactions with either Glu539 or Trp557 in the CRD, through ionic or cation–π interactions. To further validate the role of this interface in the propagation of signals to the 7TM domain, we generated ECL2 mutants of full-length mGlu5 as well as of a truncated mGlu5 construct that encodes the 7TM domain alone. Previous work has shown that an isolated mGlu5 transmembrane domain functions similarly to rhodopsin-like receptors, with PAMs and NAMs acting analogously to orthosteric agonists and antagonists at family A GPCRs<sup>11</sup>. Deletion of residues Ile726 and Arg727 at the apex of ECL2 markedly reduces the orthosteric agonist action of L-glutamate and (S)-3,5-dihydroxyphenylglycine ((S)-3,5-DHPG) in the full-length receptor (Fig. 6b, Supplementary Fig. 2, Supplementary Table 4); however, it has only a small effect on the action of CDPPB in the full-length receptor (Fig. 6c, Supplementary Table 4), and no effect on CDPPB activation of the 7TM domain alone (Fig. 6d, Supplementary Table 4). We note that surface expression levels—as well as total expression levels—of the ECL2-I726-R727 deletion mutant were comparable to those of the wild type, but that further truncation of ECL2 compromised surface expression (Supplementary Fig. 3). Deletion of I726 and R727 in ECL2 did not affect the respective constitutive activities of the full-length receptor and 7TM domain constructs (Supplementary Fig. 2). The reduction in maximal signalling response with orthosteric agonists of the ECL2-I726-R727 deletion mutant suggests that ECL2 may serve as a rigid fulcrum that aids in the propagation of agonist-induced conformational changes at the VFT to the signalling domain in the membrane. It is likely that, in the absence of this ECL2 interaction, the loop at the boundary of the CRD and TM1 does not have the rigidity to relay the conformational change to the 7TM domain, and is therefore unable to direct the structural rearrangements that lead to the formation of the active TM6 interface.

### Discussion

The combination of our in vitro data, crystal structures and cryo-EM structures of mGlu5 enable us to propose a structural framework for mGlu5 activation. Agonists stabilize a compact VFT conformation that is characterized by a relatively small intersubunit bottom-lobe distance. The proximity of these bottom lobes is propagated through the CRDs to the 7TM domains, which reorient to form a TM6-mediated interface that is signalling-competent. The geometry of this structural rearrangement is crucial, as only certain intersubunit CRD crosslinks have been shown to increase receptor activity<sup>5</sup>. Similar rearrangements have been observed in other class C GPCRs, suggesting that a conformational transition by which the TM domains come into close proximity may be a hallmark of activation in this family<sup>34,35</sup>.

We identified ECL2 as necessary to relay the agonist-induced conformational changes to the 7TM domain, as it provides a second, rigid attachment point between the ECD and transmembrane domains. We therefore propose that the ECL2–CRD interaction is the structural basis for the allosteric that has been observed between the ECD and the 7TM domain<sup>36,37</sup>. Although our results do not fully explain how agonist binding at the VFT leads to G protein coupling and activation, they do support a model in which both inter- and intrasubunit rearrangements are required for full activity<sup>5</sup>. This work addresses the first of these conformational changes. Further studies are required to elucidate the mechanism by which the establishment of a TM6–TM6 interface leads to transmembrane domain rearrangements that enable G protein coupling and signalling.

### Online content

Any methods, additional references, Nature Research reporting summaries, source data, statements of data availability and associated accession codes are available at <https://doi.org/10.1038/s41586-019-0881-4>.

Received: 11 September 2018; Accepted: 12 December 2018;  
Published online 23 January 2019.

1. Niswender, C. M. & Conn, P. J. Metabotropic glutamate receptors: physiology, pharmacology, and disease. *Annu. Rev. Pharmacol. Toxicol.* **50**, 295–322 (2010).
2. Pin, J.-P. & Bettler, B. Organization and functions of mGlu and GABA<sub>B</sub> receptor complexes. *Nature* **540**, 60–68 (2016).
3. Kunishima, N. et al. Structural basis of glutamate recognition by a dimeric metabotropic glutamate receptor. *Nature* **407**, 971–977 (2000).
4. Knaiazeff, J. et al. Closed state of both binding domains of homodimeric mGlu receptors is required for full activity. *Nat. Struct. Mol. Biol.* **11**, 706–713 (2004).
5. Hlavackova, V. et al. Sequential inter- and intrasubunit rearrangements during activation of dimeric metabotropic glutamate receptor 1. *Sci. Signal.* **5**, ra59 (2012).
6. Wu, H. et al. Structure of a class C GPCR metabotropic glutamate receptor 1 bound to an allosteric modulator. *Science* **344**, 58–64 (2014).
7. Doré, A. S. et al. Structure of class C GPCR metabotropic glutamate receptor 5 transmembrane domain. *Nature* **511**, 557–562 (2014).
8. Christopher, J. A. et al. Fragment and structure-based drug discovery for a class C GPCR: discovery of the mGlu<sub>5</sub> negative allosteric modulator HTL14242 (3-chloro-5-[6-(5-fluoropyridin-2-yl)pyrimidin-4-yl]benzonitrile). *J. Med. Chem.* **58**, 6653–6664 (2015).
9. Christopher, J. A. et al. Structure-based optimization strategies for G protein-coupled receptor (GPCR) allosteric modulators: a case study from analyses of new metabotropic glutamate receptor 5 (mGlu<sub>5</sub>) X-ray structures. *J. Med. Chem.* <https://doi.org/10.1021/acs.jmedchem.7b01722> (2018).
10. Thal, D. M., Glukhova, A., Sexton, P. M. & Christopoulos, A. Structural insights into G-protein-coupled receptor allostery. *Nature* **559**, 45–53 (2018).
11. Goudet, C. et al. Heptahelical domain of metabotropic glutamate receptor 5 behaves like rhodopsin-like receptors. *Proc. Natl Acad. Sci. USA* **101**, 378–383 (2004).
12. El Moustaine, D. et al. Distinct roles of metabotropic glutamate receptor dimerization in agonist activation and G-protein coupling. *Proc. Natl Acad. Sci. USA* **109**, 16342–16347 (2012).
13. Manglik, A., Kobikia, B. K. & Steyaert, J. Nanobodies to study G protein-coupled receptor structure and function. *Annu. Rev. Pharmacol. Toxicol.* **57**, 19–37 (2017).
14. Kinney, G. G. et al. A novel selective positive allosteric modulator of metabotropic glutamate receptor subtype 5 has *in vivo* activity and antipsychotic-like effects in rat behavioral models. *J. Pharmacol. Exp. Ther.* **313**, 199–206 (2005).
15. Gregory, K. J. et al. Investigating metabotropic glutamate receptor 5 allosteric modulator cooperativity, affinity, and agonism: enriching structure-function studies and structure-activity relationships. *Mol. Pharmacol.* **82**, 860–875 (2012).
16. Bradley, S. J., Langmead, C. J., Watson, J. M. & Challiss, R. A. J. Quantitative analysis reveals multiple mechanisms of allosteric modulation of the mGlu5 receptor in rat astroglia. *Mol. Pharmacol.* **79**, 874–885 (2011).
17. Noetzel, M. J. et al. Functional impact of allosteric agonist activity of selective positive allosteric modulators of metabotropic glutamate receptor subtype 5 in regulating central nervous system function. *Mol. Pharmacol.* **81**, 120–133 (2012).
18. Bradley, S. J., Watson, J. M. & Challiss, R. A. J. Effects of positive allosteric modulators on single-cell oscillatory Ca<sup>2+</sup> signaling initiated by the type 5 metabotropic glutamate receptor. *Mol. Pharmacol.* **76**, 1302–1313 (2009).
19. Doumazane, E. et al. Illuminating the activation mechanisms and allosteric properties of metabotropic glutamate receptors. *Proc. Natl Acad. Sci. USA* **110**, E1416–E1425 (2013).
20. Chappell, M. D. et al. Discovery of (1S,2R,3S,4S,5R,6R)-2-amino-3-[(3,4-difluorophenyl)sulfanyl]methyl]-4-hydroxy-bicyclo[3.1.0]hexane-2,6-dicarboxylic acid hydrochloride (LY3020371·HCl): A potent, metabotropic glutamate 2/3 receptor antagonist with antidepressant-like activity. *J. Med. Chem.* **59**, 10974–10993 (2016).
21. Huang, S. et al. Interdomain movements in metabotropic glutamate receptor activation. *Proc. Natl Acad. Sci. USA* **108**, 15480–15485 (2011).
22. Siméon, F. G. et al. Synthesis and simple <sup>18</sup>F-labeling of 3-fluoro-5-(2-(fluoromethyl)thiazol-4-yl)ethynylbenzonitrile as a high affinity radioligand for imaging monkey brain metabotropic glutamate subtype-5 receptors with positron emission tomography. *J. Med. Chem.* **50**, 3256–3266 (2007).
23. Muto, T., Tsuchiya, D., Morikawa, K. & Jingami, H. Structures of the extracellular regions of the group II/III metabotropic glutamate receptors. *Proc. Natl Acad. Sci. USA* **104**, 3759–3764 (2007).
24. Ray, K. & Hauschild, B. C. Cys-140 is critical for metabotropic glutamate receptor-1 dimerization. *J. Biol. Chem.* **275**, 34245–34251 (2000).
25. Manglik, A. et al. Structural insights into the dynamic process of β<sub>2</sub>-adrenergic receptor signaling. *Cell* **161**, 1101–1111 (2015).
26. Rosenbaum, D. M. et al. Structure and function of an irreversible agonist-β<sub>2</sub> adrenoceptor complex. *Nature* **469**, 236–240 (2011).
27. Levitz, J. et al. Mechanism of assembly and cooperativity of homomeric and heteromeric metabotropic glutamate receptors. *Neuron* **92**, 143–159 (2016).
28. Stenkamp, R. E. Identifying G protein-coupled receptor dimers from crystal packings. *Acta Crystallogr. D* **74**, 655–670 (2018).
29. Milligan, G. G protein-coupled receptor hetero-dimerization: contribution to pharmacology and function. *Br. J. Pharmacol.* **158**, 5–14 (2009).
30. James, J. R., Oliveira, M. I., Carmo, A. M., laboni, A. & Davis, S. J. A rigorous experimental framework for detecting protein oligomerization using bioluminescence resonance energy transfer. *Nat. Methods* **3**, 1001–1006 (2006).
31. Xue, L. et al. Major ligand-induced rearrangement of the heptahelical domain interface in a GPCR dimer. *Nat. Chem. Biol.* **11**, 134–140 (2015).
32. Isberg, V. et al. Generic GPCR residue numbers – aligning topology maps while minding the gaps. *Trends Pharmacol. Sci.* **36**, 22–31 (2015).
33. Rondard, P., Rovira, X., Goudet, C. & Pin, J.-P. in *mGLU Receptors* (ed. Ngomba, R.T. et al.) 129–147 (Springer, Cham, 2017).
34. Geng, Y., Bush, M., Mosyak, L., Wang, F. & Fan, Q. R. Structural mechanism of ligand activation in human GABA<sub>B</sub> receptor. *Nature* **504**, 254–259 (2013).
35. Geng, Y. et al. Structural mechanism of ligand activation in human calcium-sensing receptor. *eLife* **5**, e13662 (2016).
36. Martín, M., Sanz, J. M. & Cubero, A. Characterization of metabotropic glutamate receptors coupled to a pertussis toxin sensitive G-protein in bovine brain coated vesicles. *FEBS Lett.* **316**, 191–196 (1993).
37. Doornbos, M. L. J. et al. Molecular mechanism of positive allosteric modulation of the metabotropic glutamate receptor 2 by JNJ-46281222. *Br. J. Pharmacol.* **173**, 588–600 (2016).

**Acknowledgements** The work is supported by National Institutes of Health (NIH) grant R01 NS092695 (G.S., B.K.K. and J.M.M.) and NIH grant R01 NS028471 (B.K.K.). Research reported in this publication was supported by the National Institute of General Medical Sciences (NIGMS) of the NIH under award number T32GM007276 (A.K.). R.F. is funded by grant NNF15OC0015268 from the Novo Nordisk Foundation and the Stanford Bio-X Program. We thank H. Lundbeck for the synthesis of FFMTEB. This research used resources of the Advanced Photon Source, a US Department of Energy (DOE) Office of Science User Facility operated for the DOE Office of Science by Argonne National Laboratory under contract no. DE-AC02-06CH11357. Use of the Stanford Synchrotron Radiation Lightsource (SSRL), SLAC National Accelerator Laboratory, is supported by the DOE under contract no. DE-AC02-76SF00515. The SSRL Structural Molecular Biology Program is supported by the DOE Office of Biological and Environmental Research, and by the NIGMS (including P41GM103393). The content is solely the responsibility of the authors and does not necessarily represent the official view of the National Institutes of Health. B.K.K. is a Chan Zuckerberg Biohub Investigator.

**Reviewer information** *Nature* thanks K. Gregory, J.-P. Pin and J. Rubinstein for their contribution to the peer review of this work.

**Author contributions** A.K. developed purification schemes and purified all proteins for cryo-EM studies as well as mGlu5 ECD constructs for crystallography, obtained the ECD crystals with Nb43 and solved their structures, built and refined models of full-length mGlu5 from cryo-EM data, and wrote the manuscript. H.H. prepared cryo-EM grids, collected and processed cryo-EM data, and assisted with manuscript preparation. D.F. developed the purification protocol for crystallization of full-length mGlu5, obtained crystals of full-length mGlu5 and prepared mGlu5 samples for immunization. B.S. collected crystals of full-length mGlu5, collected and processed diffraction data and refined the model with assistance from M.C. and A.K. T.S.K. supervised D.F., B.S. and M.C. Y.Z. screened conditions for freezing cryo-EM grids of mGlu5. M.J.R. performed molecular dynamics simulations of mGlu5. T.L. and J.S. performed llama immunization, cDNA production, and selections by phage display. S.D. and J.T. performed early characterizations of mGlu5 by electron microscopy and helped to develop purification schemes. R.F. assisted with model building. W.I.W. assisted with model building, refinement and interpretation of all structures. J.M.M. conceived and performed all *in vitro* characterizations of ligands, mGlu5 constructs and mutants, and co-wrote the manuscript. G.S. and B.K.K. supervised the project and co-wrote the manuscript.

**Competing interests** B.K.K. and T.S.K. are founders of and consultants for ConformetRx, Inc. D.F. and B.S. are employees of ConformetRx, Inc., and M.C. is a former employee of ConformetRx, Inc.

#### Additional information

**Extended data** is available for this paper at <https://doi.org/10.1038/s41586-019-0881-4>.

**Supplementary information** is available for this paper at <https://doi.org/10.1038/s41586-019-0881-4>.

**Reprints and permissions information** is available at <http://www.nature.com/reprints>.

**Correspondence and requests for materials** should be addressed to J.M.M. or G.S. or B.K.K.

**Publisher's note:** Springer Nature remains neutral with regard to jurisdictional claims in published maps and institutional affiliations.

## METHODS

No statistical methods were used to predetermine sample size. The experiments were not randomized and the investigators were not blinded to allocation during experiments and outcome assessment.

**Purification of mGlu5 ECD.** A construct encoding residues 21–569 of wild-type human mGlu5 followed by a hexahistidine tag was cloned into the insect cell secretion vector pACGP67 and used to generate Baculovirus using the BestBac method (Expression Systems). Hi-Five (*Trichoplusia ni*) cells were infected with baculovirus at a density of  $3.5 \times 10^6$  cells per ml for 72 h at 27 °C. Cells were removed from the medium by centrifugation at 3,360g, at which point the medium was quenched of chelating agents by addition of 1 mM NiCl<sub>2</sub> and 5 mM CaCl<sub>2</sub> with rapid stirring at 25 °C for 1 h. Precipitates were removed from the medium by centrifugation at 3,360g. The pH of the medium was balanced by the addition of Tris pH 8.0 (to a final concentration of 50 mM) before loading over 5 ml of Ni-NTA resin. Resin was washed in 500 mM NaCl, 20 mM HEPES pH 7.5 and 20 mM imidazole, then in 100 mM NaCl, 20 mM HEPES pH 7.5 and 20 mM imidazole. Protein was eluted in 100 mM NaCl, 20 mM HEPES pH 7.5 and 250 mM imidazole, after which fractions containing ECD were pooled, and the His tag was removed by the addition of carboxypeptidase A and B during overnight dialysis into 100 mM NaCl, 20 mM HEPES pH 7.5 at 4 °C. Contaminants and uncleaved protein were separated by flowing over Ni-NTA resin and the flow-through was collected. The protein was finally purified by size-exclusion chromatography on a Superdex 200 10/30 column in 100 mM NaCl with 20 mM HEPES pH 7.5. Monomeric fractions were pooled and concentrated to 30 mg ml<sup>-1</sup> and flash-frozen in liquid nitrogen.

**Purification of Nb43 for signalling studies and crystallography.** Nb43 was cloned into a modified pE-SUMO vector containing a PelB leader sequence and AAA linker in front of the SUMO fusion tag. Transformed BL21 *Escherichia coli* were grown to an optical density at 600 nm (OD<sub>600</sub>) of about 0.6 at 37 °C and induced with 1 mM IPTG, and transferred to 25 °C shakers in which induction was allowed to run overnight. Bacteria were collected by centrifugation and frozen. Nb43 was purified from the periplasm using established protocols. In brief, cells were thawed in two volumes SET buffer (0.5 M sucrose, 0.5 mM EDTA, 0.2 M Tris pH 8.0) and stirred until homogenized before the addition of 3 volumes of 25 °C Milli-Q water with rapid stirring for 45 min to release periplasmic contents. Cell debris was removed by centrifugation at 24,400g for 20 min. Before loading over Ni-NTA resin, 100 mM NaCl and 10 mM MgCl<sub>2</sub> were added to provide ionic strength and to quench EDTA, respectively. After loading the quenched sample, resin was washed in 500 mM NaCl, 20 mM HEPES pH 7.5 and 20 mM imidazole, then in 100 mM NaCl, 20 mM HEPES pH 7.5 and 20 mM imidazole. Protein was eluted in 100 mM NaCl, 20 mM HEPES pH 7.5 and 250 mM imidazole, fractions containing SUMO-Nb43 were pooled, and His-SUMO tags were removed by the addition of ULP1. Imidazole was removed by overnight dialysis into 100 mM NaCl, 20 mM HEPES pH 7.5 at 4 °C. Contaminants and uncleaved protein were separated by flowing over Ni-NTA resin and the flow-through was collected. Nb43 was finally purified by size-exclusion chromatography on a Superdex 200 10/30 column in 100 mM NaCl with 20 mM HEPES pH 7.5. Monomeric fractions were pooled and concentrated to 98 mg ml<sup>-1</sup> (around 3 mM) and flash-frozen in liquid nitrogen. Nb43 purified in this manner was used for both structural and pharmacological studies.

**Crystallization of the apo ECD in complex with Nb43 and data collection.** mGlu5 ECD was incubated with 1.2 molar excess Nb43 for 30 min at 25 °C and excess Nb43 was removed by size-exclusion chromatography on a Superdex 200 10/30 column in 100 mM NaCl with 20 mM HEPES pH 7.5. Fractions containing complex were pooled and concentrated to 20 mg ml<sup>-1</sup> and flash-frozen in liquid nitrogen.

Initial crystallization hits were identified in around 30% of conditions in commercial screens, and a refined condition containing 18–20% PEG 3350, 0.15 M potassium nitrate, with 1% benzamidine gave final crystals. These crystals were cryoprotected in reservoir solution + 25% glycerol and frozen in liquid nitrogen.

Data were collected on BL12-2 at SSRL at 100 K, processed using XDS<sup>38</sup> and scaled using AIMLESS<sup>39</sup> in the CCP4<sup>40</sup> suite. Phases were obtained by molecular replacement, using individual top and bottom VFT lobes from a structure of the mGlu5 VFT bound to glutamate (PDB: 3LMK). A homology model of Nb43 was generated using Swiss-Model<sup>41</sup> and manually placed in positive density after refinement to the VFT alone. The model was iteratively refined using PHENIX<sup>42</sup> and manually in Coot<sup>43</sup> and showed good stereochemistry, with 94.95% of residues in Ramachandran favoured zones, 4.97% in allowed zones and 0.08% outliers.

**Crystallization of the ECD in complex with quisqualate and Nb43.** mGlu5 ECD in complex with Nb43 was incubated with a tenfold molar excess of L-quisqualic acid (Tocris) for 30 min at 25 °C and initial crystallization hits were identified using commercial screens. Crystals reproducibly emerged in 100 mM NaCl with 20% PEG species at a range of pH values. Final crystals were grown in 100 mM NaCl, 50 mM ADA buffer pH 7.0 and 20% PEG 4000. Crystals were cryoprotected in reservoir solution plus 25% glycerol and frozen in liquid nitrogen.

Data were collected on Beamline 23 IDB at the Advanced Photon Source (APS) at Argonne National Laboratories and processed using XDS<sup>38</sup> and AIMLESS<sup>39</sup> from the CCP4<sup>40</sup> package. Phases were obtained by molecular replacement using a structure of the mGlu5 VFT bound to glutamate (PDB: 3LMK), and nanobodies were placed using the structure of the apo ECD in complex with Nb43. Model building was performed manually in Coot<sup>43</sup> and refined using PHENIX<sup>42</sup> and BUSTER<sup>44,45</sup>. The final model showed good stereochemistry, with 94.66% of residues in Ramachandran favoured zones, 5.34% in allowed zones and 0% outliers. **Expression, purification and crystallization of full-length mGlu5 bound to NAM FFMTEB.** The haemagglutinin (HA) signal peptide, followed by a Flag epitope tag (DYKDDDD) and a three-alanine linker, was added to the N terminus of unmodified human mGlu5 (21–865) with a hexahistidine tag at the C terminus. This construct was cloned into the pFastBac1 sf9 expression vector and recombinant baculovirus was prepared using the Bac-to-Bac baculovirus expression system (Invitrogen). SF9 insect cells were infected with the virus at a cell density of  $3.5 \times 10^6$  cells per ml and grown for 48 h at 27 °C with gentle rotation.

Cells were collected by centrifugation, and lysed by resuspension in hypotonic buffer containing 10 mM Tris at pH 7.8 and 1 mM EDTA with protease inhibitors followed by homogenization. The cell membrane pellet was collected by centrifugation and was solubilized with 1% (w/v) n-dodecyl-β-D-maltoside (DDM) (Anatrace), 0.1% (w/v) cholesterol hemisuccinate (CHS) (Steraloids), 0.2% (w/v) sodium cholate (Anatrace), 750 mM NaCl, 30% glycerol, iodoacetamide (2 mg ml<sup>-1</sup>), protease inhibitor and 10 μM FFMTEB (compound 3 in ref.<sup>22</sup>) (a gift from H. Lundbeck). FFMTEB (3-fluoro-5-(2-(2-(fluoromethyl)thiazol-4-yl)ethynyl)benzonitrile) is a fluorinated analogue of F-MTEB with exceptionally high affinity and selectivity for mGlu5. The supernatant was isolated and incubated with anti-Flag M1 affinity resin (Sigma) overnight at 4 °C. The resin was washed with 0.1% (w/v) DDM, 0.01% (w/v) CHS, 500 mM NaCl, 10% glycerol and 10 μM FFMTEB, followed by 0.1% (w/v) lauryl maltose neopentyl glycol (LMNG), 0.01% (w/v) CHS, 150 mM NaCl and 10 μM AF57974 buffer to exchange the detergent. mGlu5 bound to FFMTEB was eluted in 30 mM HEPES pH 7.5, 150 mM NaCl, 0.01% (w/v) MNG, 0.01% (w/v) CHS, 200 μg ml<sup>-1</sup> Flag peptide, 5 mM EDTA and 10 μM FFMTEB. The protein was concentrated in a 50-kDa cutoff Vivaspin (Millipore) filter and run on a Superdex 200 size-exclusion column (GE Healthcare).

Purified mGlu5 receptor was concentrated to 20 mg ml<sup>-1</sup> and crystallized using the vapour-phase diffusion method. Protein was mixed with precipitant solution at a 1:1 ratio in sitting drops, using a Gryphon Crystallography Robot (Art Robbins Instrument) for setups. The crystals that were used for data collection were grown in 15% PEG 3350 (w/v), 0.2 M sodium cacodylate pH 6.5 at 20 °C in a 24-well plate (Hampton Research). Crystals were cryoprotected by adding glycerol in a stepwise manner to reach a final concentration of 30%, and then flash-frozen in liquid nitrogen.

**X-ray data collection, processing and structure determination of full-length mGlu5 bound to the NAM FFMTEB.** X-ray diffraction data were collected at APS at GM/CA beamline 23ID-D and 23ID-B. Even though the crystals were of sufficient size (>0.2 mm), usually only a particular small region yielded suitable diffraction. The entire crystal was therefore first screened by rastering using a 40 μm × 40 μm-beam with fivefold attenuation and 0.5-s exposure. Regions that contained the strongest diffraction were then sub-rastered using a 20-μm collimated beam with fivefold attenuation. Data were then collected with the 20-μm beam using two- to fivefold attenuation with 1–2-s exposures and 0.2-degree oscillations. Owing to radiation damage, data was collected in wedges of 5–25 degrees before moving onto either a different site on the crystal or a new crystal. Diffraction data were processed using XDS<sup>38</sup> and statistics are summarized in Extended Data Table 1. The structure was solved by molecular replacement using Phaser with the mGlu5 VFT domain structure in an open conformation (from the structure of apo ECD in complex with Nb43, but with Nb43 removed) as the search model. The resulting model was completed by iterative refinement in PHENIX<sup>42</sup>, Refmac<sup>46</sup> and BUSTER<sup>44,45</sup> and manual building with Coot<sup>43</sup>. MolProbity<sup>47</sup> was used for structure validation, and figures were prepared using PyMOL (Schrödinger). Final refinement statistics are reported in Extended Data Table 1. In short, despite the limited resolution, we were able to refine a model with excellent stereochemistry (94% Ramachandran favoured, 5.9% Ramachandran allowed and 0.1% outliers) and well-defined electron density for the main chain and the majority of the side chains.

**Liposome reconstitution and llama immunization.** The mGlu5 full-length receptor was purified as described above. The resulting receptor was reconstituted into phospholipid vesicles composed of 1,2-dioleoyl-sn-glycerol-3-phosphocholine (DOPC, Avanti Polar Lipids) and lipid A (Avanti Polar Lipids) in a 10:1 ratio at a final receptor concentration of 1 mg ml<sup>-1</sup>. The reconstituted receptor was flash-frozen in liquid nitrogen in 100 μg aliquots for llama immunization. One llama was immunized over 6 weeks with 0.25 mg of liposome-reconstituted mGlu5. Peripheral blood lymphocytes were isolated from the llama to extract total RNA, prepare cDNA and construct a nanobody phage-display library as previously described<sup>48</sup>. Animal studies were performed under ethical guidelines outlined by

European Union animal welfare legislation and a local ethical committee for use of laboratory animals of the Vrije Universiteit Brussels.

**Preparation of mGlu5 membranes for cryo-EM studies.** The HA-Flag-human mGlu5 (21–865) construct described above was used to infect *Spodoptera frugiperda* SF9 cells at a density of 4 million cells per ml in the presence of 3-((2-methyl-4-thiazolyl)ethynyl)pyridine (MTEP). Infection continued for 60 h at 27 °C with rotation at 130 r.p.m., at which point cells were collected by centrifugation and stored at –80 °C. Membranes were prepared following established protocols. In brief, collected cell pellets were thawed and lysed in hypotonic buffer (10 mM HEPES pH 7.5, 1 mM EDTA with 160 µg ml<sup>-1</sup> benzamidine and 2.5 µg ml<sup>-1</sup> and 10 µM MTEP). Cyttoplasmic contents were separated by centrifugation, and cell remains were resuspended in a high salt buffer composed of 1 M NaCl, 20 mM HEPES pH 7.5, 160 µg ml<sup>-1</sup> benzamidine, 2.5 µg ml<sup>-1</sup> leupeptin and 10 µM MTEP) using a tissue shearer (Polytron). Fine membrane particulates were pelleted by ultracentrifugation at 220,000*g* in a Ti-45 rotor for 60 min and pellets were topped with 100 mM NaCl, 20 mM Tris pH 7.5, 10 µM MTEP, 30% glycerol before flash-freezing in liquid nitrogen.

**Preparation of the MTEP-bound mGlu5 in nanodiscs.** Crude membranes (described above) were thawed and solubilized in a buffer consisting of 750 mM NaCl, 20 mM HEPES pH 7.5, 1% DDM, 0.2% cholate, 0.12% CHS, 10 µM MTEP<sup>49</sup>, 160 µg ml<sup>-1</sup> benzamidine and 2.5 µg ml<sup>-1</sup> leupeptin (EMD Millipore). Solubilization proceeded for 90 min at 4 °C with constant stirring, and 1 mg ml<sup>-1</sup> iodoacetamide was added to block reactive cysteines. Insoluble material was removed by centrifugation at 37,000*g* for 25 min, at which point 2 mM calcium and 4 ml M1 anti-Flag resin was added. Batch binding occurred for 90 min at 4 °C with constant stirring.

Resin was collected by centrifugation at 3,000*g* for 2 min, and washed in batch with 500 mM NaCl, 20 mM HEPES pH 7.5, 0.1% DDM, 0.01% CHS, 2 mM CaCl<sub>2</sub> and 10 µM MTEP. Resin was transferred to an EconoPac column and washed with the same buffer, and finally with 100 mM NaCl, 20 mM HEPES pH 7.5, 0.1% DDM, 0.01% CHS, 2 mM CaCl<sub>2</sub> and 10 µM MTEP. Protein was finally eluted using 100 mM NaCl, 20 mM HEPES pH 7.5, 0.1% DDM, 0.01% CHS, 10 µM MTEP, as well as 0.2 mg ml<sup>-1</sup> Flag peptide and 5 mM EDTA. Fractions containing protein were pooled and concentrated to about 10 µM. Concentrated protein was reconstituted in MSP1D1 nanodiscs following previously published protocols<sup>50</sup>. In brief, mGlu5 was mixed with MSPD1 belt protein and lipids in the following ratio: 0.1 receptor:1 MSP1D1:65 POPC/POPG (POPC:POPG ratio 3:2). After 3 h of incubation on ice, Bio-Beads were added at a ratio of 1 mg Bio-Beads:14 mg lipid. After 1 h at 4 °C, the same amount of Bio-Beads were added again and reconstitution continued at 4 °C overnight with gentle rocking.

Reconstitution mixture was removed from beads, concentrated and injected on a Superose 6 10/30 gel-filtration column in 100 mM NaCl, 20 mM HEPES pH 7.5, 10 µM MTEP to separate aggregates and empty discs. Monomeric peak fractions were collected and concentrated to around 6 mg ml<sup>-1</sup> for imaging.

**Preparation of mGlu5 bound to CDPPB, L-quinalate and Nb43.** Crude membranes (described above) were thawed and solubilized in a buffer consisting of 750 mM NaCl, 20 mM HEPES pH 7.5, 1% DDM, 0.2% cholate, 0.12% CHS, 10 µM MTEP, 160 µg ml<sup>-1</sup> benzamidine and 2.5 µg ml<sup>-1</sup>. Solubilization proceeded for 90 min at 4 °C with constant stirring, and 1 mg ml<sup>-1</sup> iodoacetamide was added to block reactive cysteines. Insoluble material was removed by centrifugation at 37,000*g* for 25 min, at which point 2 mM calcium and 4 ml M1 anti-Flag resin was added. Batch binding occurred for 90 min at 4 °C with constant stirring.

Resin was collected by centrifugation at 3,000*g* for 2 min, and washed in batch with 500 mM NaCl, 20 mM HEPES pH 7.5, 0.1% DDM, 0.01% CHS, 2 mM CaCl<sub>2</sub> and 10 µM MTEP. Resin was transferred to an EconoPac column and washed with the same buffer. At this point, detergent was exchanged for glyco-diosgenin (GDN) by increasing the proportion of a 0.2% GDN/0.02% CHS mixture in stepwise increments and lowering the proportion of 0.1% DDM/0.01% CHS over a period of 30 min. The concentration of GDN was then lowered to 0.02% (around ten times the critical micelle concentration) in 100 mM NaCl, 20 mM HEPES, 0.02% CHS and 2 mM CaCl<sub>2</sub>, and then 5 µM CDPPB<sup>51</sup> was added to the wash buffer to exchange NAM for PAM. Ligand exchange was allowed to proceed for 20 min with buffer at 25 °C, at which point the receptor was eluted in 0.02% GDN, 0.002% CHS, 100 mM NaCl, 20 mM HEPES pH 7.5, 5 µM CDPPB supplemented with 5 mM EDTA and 0.2 mg ml<sup>-1</sup> Flag peptide. Protein-containing fractions were pooled, concentrated and mixed with a 1.2 molar excess of Nb43 before injection on a Superose 6 10/30 gel-filtration column to remove excess nanobody and aggregate. Fractions containing both mGlu5 and Nb43 were pooled and concentrated to around 10–15 mg ml<sup>-1</sup> for imaging.

**Cryo-EM data acquisition and processing.** Inactive MTEP-bound mGlu5 (3.0 µl) in nanodiscs at a concentration of 6 mg ml<sup>-1</sup> was applied to glow-discharged 200 mesh grids (Quantifoil R1.2/1.3), containing 0.0005% Amphipol A8-35 (Anatrace). A8-35 was included to aid sample vitrification, rather than an attempt to further reconstitute the receptor into amphipol. Excess sample was removed

by blotting before plunge-freezing using a Vitrobot Mark IV (Thermo Fisher Scientific) at 4 °C and 100% humidity. Cryo-EM samples of mGlu5 in complex with Nb43, and mGlu5 in complex with Nb43 and L-quinalate in GDN were prepared similarly with the addition of 0.1% octylglucoside (OG). Cryo-EM images were collected on a Titan Krios operated at 300 kV at a nominal magnification of 130,000× with a Gatan GIF Quantum LS Imaging energy filter using a Gatan K2 Summit direct electron camera in counting mode, corresponding to a pixel size of 1.06 Å. Each image was dose-fractionated over 40 frames with a dose rate of 7 electrons per pixel per second and total exposure time of 8 s, resulting in an accumulated dose of 50 electrons per Å<sup>2</sup>. The defocus range was set to 1.2–2.5 µm. The datasets of inactive mGlu5, inactive mGlu5 in complex with Nb43, and active mGlu5 in complex with Nb43 and L-quinalate included 5,391, 7,414 and 1,984 micrographs, respectively. Dose-fractionated image stacks were subjected to beam-induced motion correction and dose-weighting using MotionCor2<sup>52</sup>. Contrast transfer function parameters for each micrograph were determined by Gctf v1.06<sup>53</sup>.

Data processing of inactive mGlu5 was performed in RELION2.1<sup>54</sup>. A subset of 618,306 particle projections from well-defined averages was selected after two rounds of 2D reference-free classification starting with 1.6 million particles. This group was subjected to two rounds of 3D classifications with a pixel size of 2.12 Å. A selected subset of 123,096 projections was used to obtain the final map with RELION using a pixel size of 1.06 Å and C<sub>2</sub> symmetry imposed in the last rounds of refinement. This map has an indicated global resolution of 4.0 Å at a Fourier shell correlation (FSC) of 0.143. The dataset of mGlu5 in complex with Nb43 (inactive) was similarly processed in RELION, with a subset of 44,831 particle projections producing a map with indicated 7.9 Å resolution. The dataset of mGlu5 in complex with Nb43 and L-quinalate (active) was preprocessed and sorted by 2D classification in RELION, resulting in 748,593 particles in well-defined averages. This subset of particle projections was exported to cryoSPARC<sup>55</sup> for further 2D and 3D classification. After two rounds of 3D classification in cryoSPARC, the angular and translational parameters for a selected group of 256,884 particles were imported to RELION for 3D classification without alignment. The final dataset of 73,472 particle projections was used in RELION to obtain a map with indicated global resolution of 4.0 Å. The final resolution estimate was based on the FSC between two unfiltered half-maps. Local resolution was determined using the Bsoft package<sup>56</sup> with unfiltered half-maps as input.

**Molecular dynamics simulations.** The nanobody–VFT-domain complex and the VFT domain alone were prepared for molecular dynamics simulations with the Maestro software (Schrödinger) to add any missing side chains or hydrogens. Protonation state and hydrogen bonding were also optimized. VMD<sup>57</sup> was then used to generate input files for NAMD<sup>58</sup> with the OPLS-AA/M force field for proteins<sup>59</sup>. Implicit solvent molecular dynamics simulations were run with NAMD using the generalized Born method with an α-cutoff of 14 Å. Smoothing at 14 Å and a cutoff at 16 Å were applied to the nonbonded interactions. Temperature was maintained at 300 K with a Langevin thermostat using a damping coefficient of 1 ps<sup>-1</sup>. A 1-fs time step was used with the SHAKE algorithm. Harmonic restraints were placed on all Cα before the system was minimized for 5,000 steps and gradually heated from 0 to 300 K in 20 K intervals ran for 50 ps each. Restraints were then removed and simulations were run for 25 ns. Four trajectories were run for each system with different initial random number seeds. The results of these replicates were used to obtain error bars for measured quantities.

**Molecular pharmacology methods. Constructs.** The mGlu5 used for the studies consisted of the human mGlu5 with the signal peptide replaced by an extended HA-signal peptide and Flag-sequence (MKTIIIALSYIFCLVFA-DYKDDDDAAA) before the mature mGlu5 sequence starting at amino acid Q21 (Uniprot P41594-2). Furthermore, part of the C terminus was removed by introducing a 6×His tag after amino acid L865. The mGlu5 construct (termed mGlu5-wt) was subcloned into pcDNA3.1(+)-neo.

An ECD-truncated construct encoding the helical domain of mGlu5 was generated by introducing the HA-Flag tag and the first 20 residues of beta2AR in front of the mGlu5 helical domain from residues D565 to L865 followed by a 6×His tag. The constructs were subcloned into pcDNA3.1(+)-neo and termed m5-HD. Introduction of the beta2AR residues rescued surface expression of the helical domain construct.

Receptor mutants were generated by site-directed mutagenesis or by overlap PCR using appropriate primers, restriction enzymes and subcloning of mutated PCR products. All constructs were sequence-verified. For the ECL2 truncation study the ECL2 residues I726–R727 (and S725–E728, P724–V729, D722–Y730) were removed by overlap PCR in full-length and ECD truncated constructs. For the TM6 mutational study the C129A, I791C, and C129A + I791C mutants were generated.

**Intracellular calcium release assay.** The day before transfection, HEK293 cells (ATCC CRL-1573) were seeded at a density of 0.6 × 10<sup>6</sup> cells in T25 flasks and a volume of 4 ml growth medium. On the day of transfection, a mixture of

2.5 µg (high expression level) or 0.05 µg (low expression level) DNA encoding each of the receptor constructs, and 2 µg of EAAT3 encoding DNA, if indicated, was incubated with 8.5 µl FuGene6 (Promega, E2692) in a total of 150 µl OptiMEM (Gibco, 51985) for 20 min at room temperature and then added to the cells. The day after transfection cells were trypsinized and seeded in black-sided, clear-bottom poly-L-lysine-coated 96-well plates at a density of 50,000 cells per well.

On the day of assay (2 days after transfection), the (glutamate-containing) growth medium was replaced with HBSS buffer (HBSS Gibco 14025, 20 mM HEPES pH 7.5, 1 mM CaCl<sub>2</sub>, 1 mM MgCl<sub>2</sub> and 0.1% BSA) supplemented with BSA to 0.5% and left in the incubator at 37°C for 4–6 h. Then cells were washed once in 100 µl HBSS buffer, and replaced with 100 µl of buffer containing Fluo-4, probenecid and 0.1% BSA (Fluo-4 Direct Calcium Assay Kit, Invitrogen, F10471). After 30 min incubation at 37°C, intracellular calcium release upon receptor activation was initiated by addition of 50 µl ligand solutions in 3 times its final concentrations to each well and read using a FLIPR Tetra High Throughput Cellular Screening System (Molecular Devices). The maximum fluorescence response from each well was used in the data analysis. Data were fitted by nonlinear regression using GraphPad Prism.

**IP1 accumulation assay.** HEK293 cells were transfected and seeded and to the point of assay initiation treated as described above except that cells were seeded in clear poly-L-lysine-coated 96-well plates. Following the wash, 50 µl HBSS buffer was added to each well. MPEP (Sigma, M5435) or buffer were preincubated by addition of MPEP or buffer in 50 µl HBSS buffer for 15 min at 37°C before adding the orthosteric and/or allosteric activating ligands (or vehicle condition) also diluted in 50 µl HBSS buffer now supplemented with LiCl to a final concentration of 20 mM. After incubation for 30 min at 37°C, the reaction was stopped by addition of 40 µl lysis buffer from the CisBio IP-One Tb HTRF Kit (CisBio, 621PAPEC). The accumulated IP1 levels were then quantified according to the manufacturer's instructions and quantified using an Envision plate reader (Perkin Elmer). Data were calculated as the amount of IP1 formed per well or normalized to the basal IP1 level and fitted by nonlinear regression using GraphPad Prism.

**Radioligand binding ([<sup>3</sup>H]L-quisqualic acid).** HEK293 cells were transfected by adding 15 µg mGlu5-wt DNA and 38 µg polyethylenimine (from 2 mg ml<sup>-1</sup> stock of Sigma-Aldrich, 408727) into a volume of 1 ml OptiMEM and incubating for 20 min at room temperature before adding the mixture to cells seeded at a density of 5 × 10<sup>6</sup> in 150 mm the day before transfection. Forty-eight hours after transfection cells were washed once and detached in DPBS supplemented with 2 mM EDTA. After pelleting, the cell pellet was resuspended in lysis buffer (50 mM HEPES pH 7.5 supplemented with cComplete, EDTA-free Protease Inhibitor Cocktail (Roche, 30307800) and homogenized using a glass douncer. The lysate was spun at 1,500 r.p.m. at 4°C for 10 min. The supernatant was then isolated and spun at 40,000g in SV-34 tubes for 20 min at 4°C. The membrane pellet was resuspended in binding buffer (50 mM HEPES pH 7.5, 150 mM NaCl, 1 mM CaCl<sub>2</sub>, 1 mM MgCl<sub>2</sub>) and frozen in aliquots at -80°C.

For saturation binding experiments 15 µg membrane protein was added together with varying concentrations of [<sup>3</sup>H]L-quisqualic acid (PerkinElmer NET1165050UC) and 10 µM Nb43 or CDPPB (Sigma, SML0235) diluted in binding buffer into 96-deepwell plates. Non-specific binding was determined by addition of 100 µM L-glutamate. For competition binding experiments 10 nM [<sup>3</sup>H]L-quisqualic acid was added together with 15 µg membrane protein and varying concentrations of L-glutamate, Nb43 or CDPPB into 96-deepwell plates. After shaking at 600 r.p.m. for 2 h at room temperature the receptor-bound radioligand was separated by filtration over Whatman GF/C unifilters (PerkinElmer, 6005174) using a 96-well FilterMate harvester (PerkinElmer). The filters were washed rapidly three times with a total of 2.5 ml of ice-cold binding buffer, and radioactivity was determined in a MicroBeta2 scintillation counter (PerkinElmer) after addition of 40 µl of MICROSCINT O (PerkinElmer, 6013611). Data were fitted by nonlinear regression using GraphPad Prism.

**Western blot.** HEK293 cells were seeded and transfected in T25 flasks as described above using FuGene6. Immediately after transfection and the day following transfection, 10 µM MPEP or corresponding vehicle was added to the growth medium during expression. Forty-eight hours after transfection cells were washed once and detached in 1 ml DPBS supplemented with 2 mM EDTA. The cells were pelleted and resuspended in 100 µl lysis buffer (10 mM Tris, pH 7.5 supplemented with cComplete, EDTA-free Protease Inhibitor Cocktail). Then cells were homogenized using a Precellys homogenizer and CK28 beads (Bertin Corp., 03961CK28) by homogenizing for 10 s at 5,000 r.p.m. and spinning of the lysate at 500g for 10 min to isolate the membrane-bound receptor. Equal amounts of receptor protein was resuspended in LDS buffer (LDS Sample Buffer, Non-Reducing (4X), Invitrogen,

NP0007) supplemented with 8% SDS (Sigma, L3771) and loaded on a NuPAGE 3–8% Tris-acetate gel (Invitrogen, EA03752BOX). Protein was blotted onto PVDF membranes (Invitrogen, LC2005), and stained first with primary Flag-M2 antibody (Sigma F3165) followed by HPR-conjugated anti-mouse antibody (Thermo Scientific, 32430). Receptor monomers and dimers were detected and quantified using a chemiluminescent substrate and a ChemiDoc imaging system, followed by Imager Laboratory 6.0 software analysis (Bio-Rad).

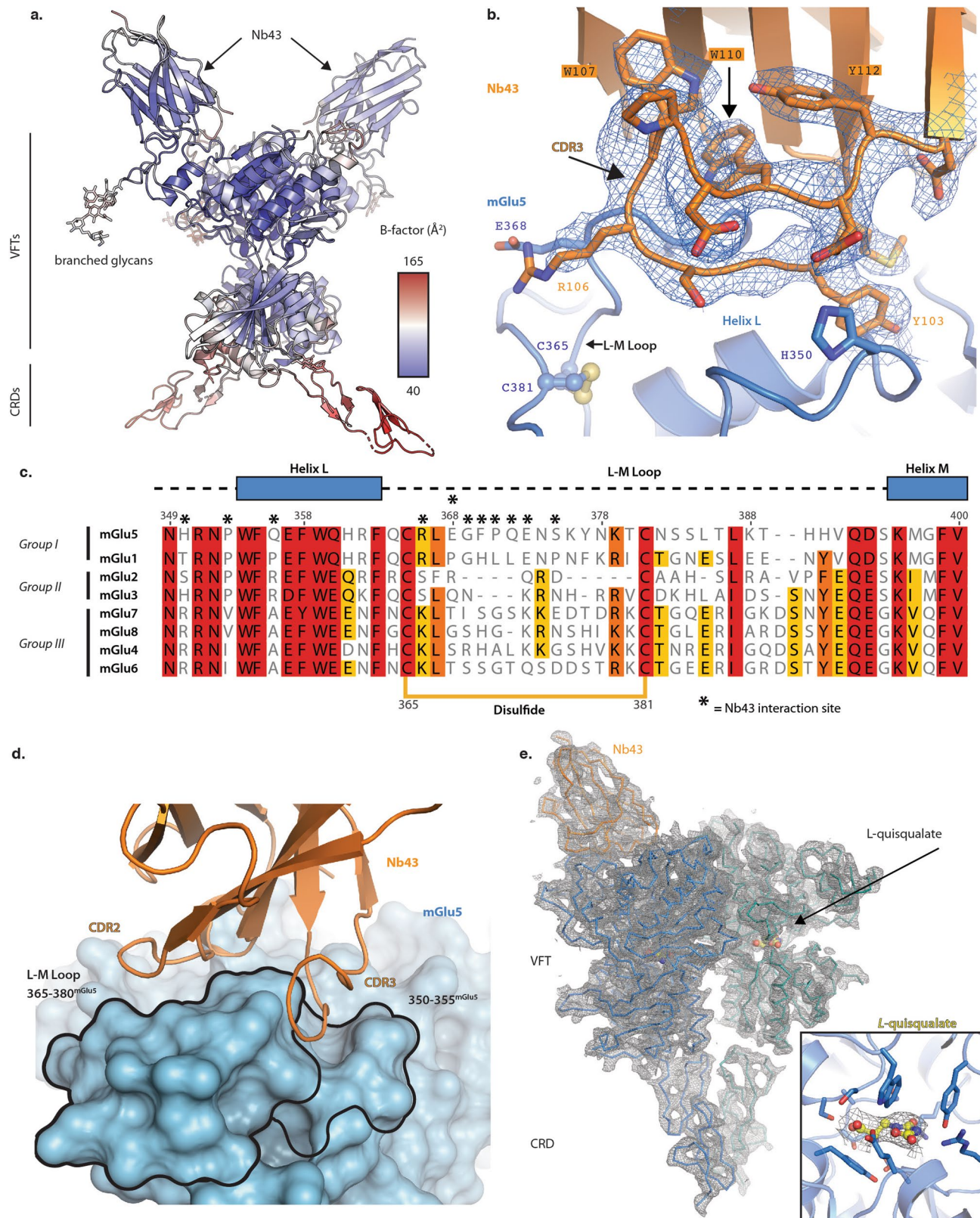
All cell lines were obtained directly from the manufacturer, but were not tested further for contamination nor re-authenticated by the authors.

**Reporting summary.** Further information on experimental design is available in the Nature Research Reporting Summary linked to this article.

## Data availability

All data generated or analysed during this study are included in this published article and its Supplementary Information. The X-ray crystal structures and structure factors of the apo mGlu5 ECD, of the apo mGlu5 ECD in complex with Nb43 and of the mGlu5 ECD in complex with Nb43 and L-quisqualate have been deposited in the Protein Data Bank under accession codes 6N4X, 6N4Y and 6N50, respectively. Cryo-EM maps of apo mGlu5 in nanodiscs, apo mGlu5 in complex with Nb43 and active mGlu5 in complex with Nb43 and L-quisqualate in GDN have been deposited in the Electron Microscopy Data Bank under accession codes EMD-0346, EMD-0347 and EMD-0345, respectively. The atomic coordinates of apo mGlu5 and active mGlu5 in complex with Nb43 and L-quisqualate have been deposited in the Protein Data Bank under accession codes 6N52 and 6N51, respectively.

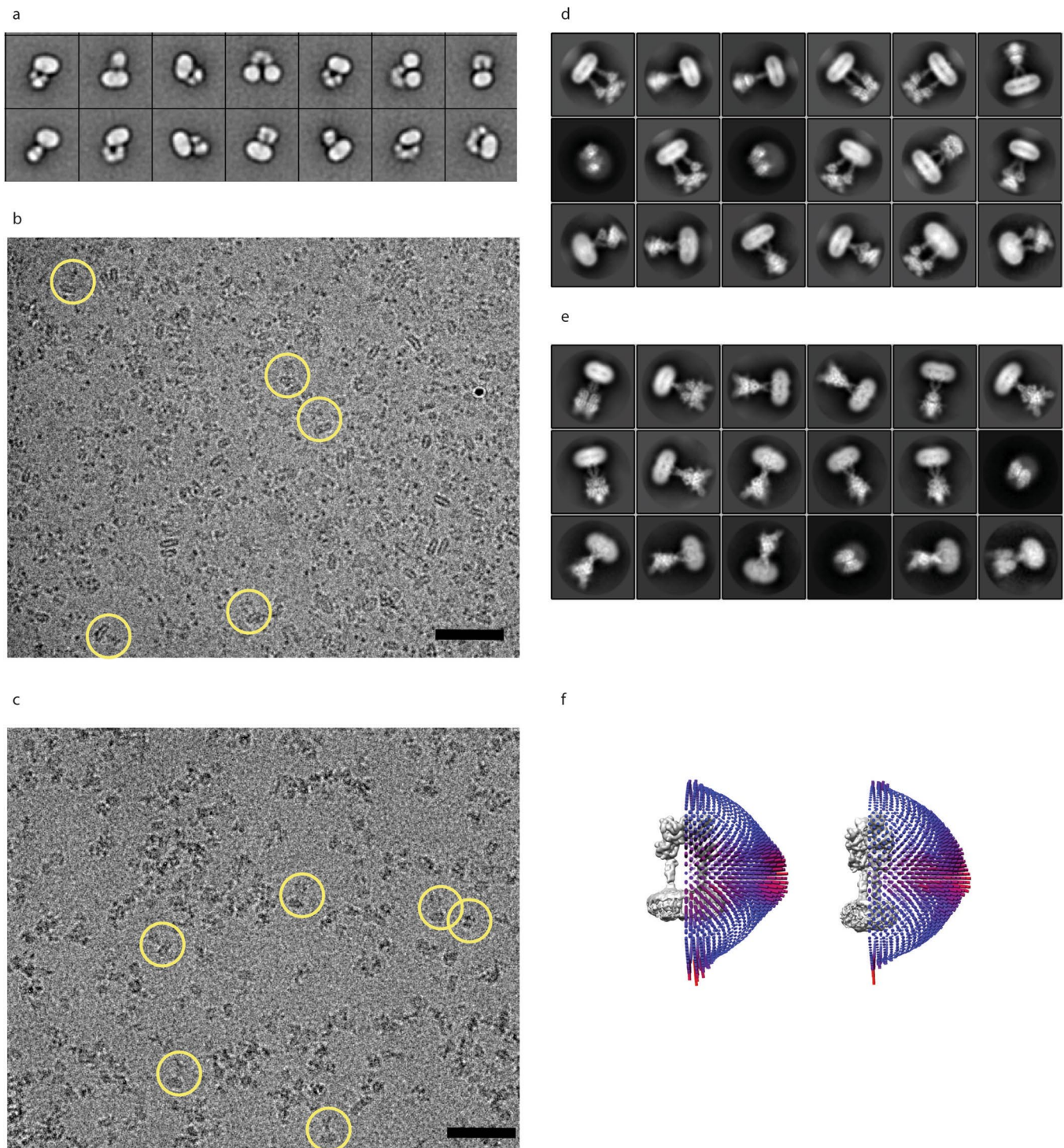
38. Kabsch, W. XDS. *Acta Crystallogr. D* **66**, 125–132 (2010).
39. Evans, P. Scaling and assessment of data quality. *Acta Crystallogr. D* **62**, 72–82 (2006).
40. Winn, M. D. et al. Overview of the CCP4 suite and current developments. *Acta Crystallogr. D* **67**, 235–242 (2011).
41. Waterhouse, A. et al. SWISS-MODEL: homology modelling of protein structures and complexes. *Nucleic Acids Res.* **46**, W296–W303 (2018).
42. Adams, P. D. et al. The Phenix software for automated determination of macromolecular structures. *Methods* **55**, 94–106 (2011).
43. Emsley, P. & Cowtan, K. Coot: model-building tools for molecular graphics. *Acta Crystallogr. D* **60**, 2126–2132 (2004).
44. Bricogne, G. et al. BUSTER v.2.10.3 (Global Phasing, Cambridge, 2017).
45. Smart, O. S. et al. Exploiting structure similarity in refinement: automated NCS and target-structure restraints in BUSTER. *Acta Crystallogr. D* **68**, 368–380 (2012).
46. Murshudov, G. N., Vagin, A. A. & Dodson, E. J. Refinement of macromolecular structures by the maximum-likelihood method. *Acta Crystallogr. D* **53**, 240–255 (1997).
47. Williams, C. J. et al. MolProbity: More and better reference data for improved all-atom structure validation. *Protein Sci.* **27**, 293–315 (2018).
48. Pardon, E. et al. A general protocol for the generation of nanobodies for structural biology. *Nat. Protoc.* **9**, 674–693 (2014).
49. Cosford, N. D. P. et al. 3-[2-Methyl-1,3-thiazol-4-yl]ethynyl]-pyridine: a potent and highly selective metabotropic glutamate subtype 5 receptor antagonist with anxiolytic activity. *J. Med. Chem.* **46**, 204–206 (2003).
50. Vélez-Ruiz, G. A. & Sunahara, R. K. Reconstitution of G protein-coupled receptors into a model bilayer system: reconstituted high-density lipoprotein particles. *Methods Mol. Biol.* **756**, 167–182 (2011).
51. Lindsley, C. W. et al. Discovery of positive allosteric modulators for the metabotropic glutamate receptor subtype 5 from a series of N-(1,3-diphenyl-1H-pyrazol-5-yl)benzamides that potentiate receptor function *in vivo*. *J. Med. Chem.* **47**, 5825–5828 (2004).
52. Zheng, S. Q., Palovcak, E., Armache, J.-P., Verba, K. A., Cheng, Y. & Agard, D. A. MotionCor2: anisotropic correction of beam-induced motion for improved cryo-electron microscopy. *Nat. Methods* **14**, 331–332 (2017).
53. Zhang, K. Gctf: Real-time CTF determination and correction. *J. Struct. Biol.* **193**, 1–12 (2016).
54. Scheres, S. H. W. RELION: implementation of a Bayesian approach to cryo-EM structure determination. *J. Struct. Biol.* **180**, 519–530 (2012).
55. Punjani, A., Rubinstein, J. L., Fleet, D. J. & Brubaker, M. A. cryoSPARC: algorithms for rapid unsupervised cryo-EM structure determination. *Nat. Methods* **14**, 290–296 (2017).
56. Heymann, J. B. & Belnap, D. M. Bsoft: image processing and molecular modeling for electron microscopy. *J. Struct. Biol.* **157**, 3–18 (2007).
57. Humphrey, W., Dalke, A. & Schulten, K. VMD: visual molecular dynamics. *J. Mol. Graph.* **14**, 33–38, 27–28 (1996).
58. Phillips, J. C. et al. Scalable molecular dynamics with NAMD. *J. Comput. Chem.* **26**, 1781–1802 (2005).
59. Robertson, M. J., Tirado-Rives, J. & Jorgensen, W. L. Improved peptide and protein torsional energetics with the OPLSAA force field. *J. Chem. Theory Comput.* **11**, 3499–3509 (2015).



Extended Data Fig. 1 | Structural basis of Nb43 binding to mGlu5.

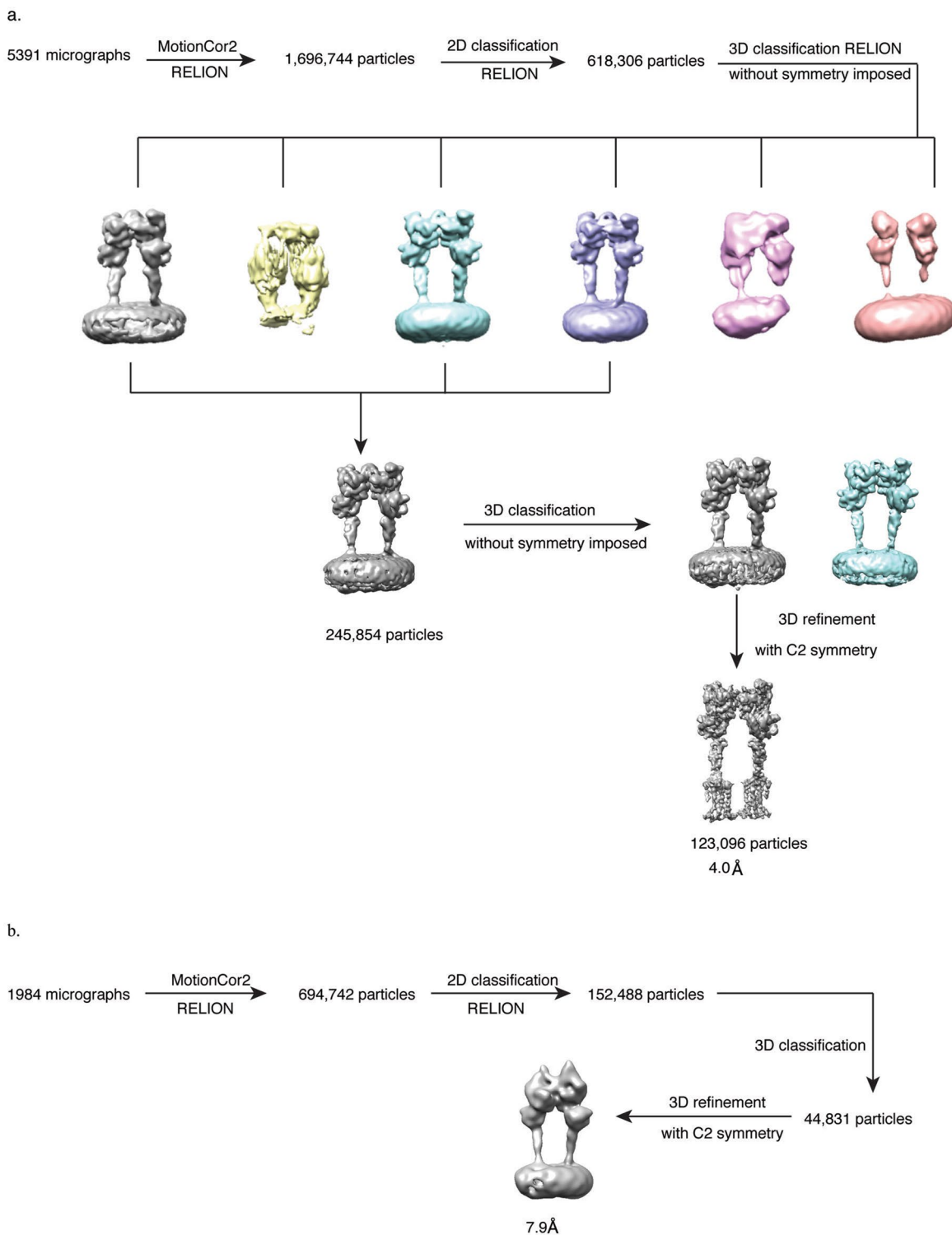
**a.** Cartoon view of the apo mGlu5 in complex with Nb43, coloured by B-factors. Notably, the CRDs are diametrically opposed and do not form a stable interface with each other, as reflected by increased B-factors relative to the VFT. **b.** The Nb43-binding interface, with a  $2F_o - F_c$  map of residues comprising CDR3 at  $1\sigma$  shown as blue mesh. **c, d.** Residues involved

in Nb43 binding are located on helix L and the L–M loop, and are not conserved. **e.** The  $2F_o - F_c$  map of the mGlu5 ECD bound to L-quisqualate and Nb43 is shown in grey mesh at  $1\sigma$  around a cartoon representation of the refined model. The inset shows the quality of density in the L-quisqualate-binding pocket.

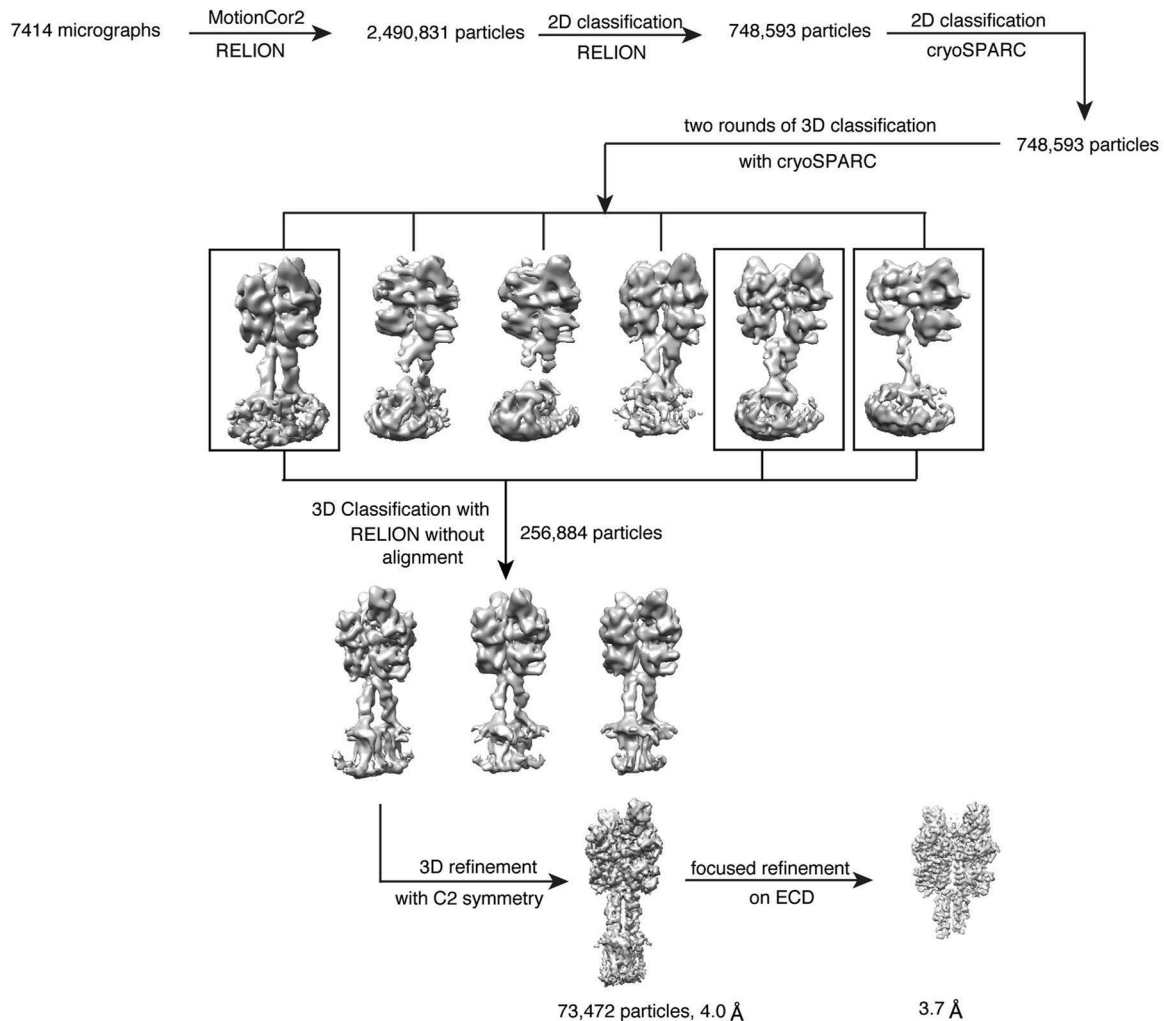
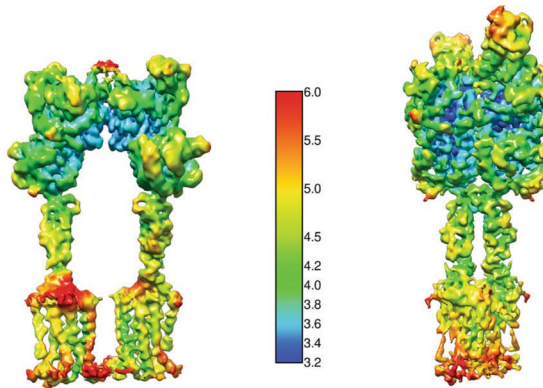


**Extended Data Fig. 2 | Overview of mGlu5 cryo-EM studies.** **a**, Two-dimensional negative-stain class averages of apo mGlu5 in LMNG shows several classes with split detergent micelles. **b, c**, Representative cryo-EM images of apo mGlu5 in nanodiscs (**b**) and active mGlu5 bound to

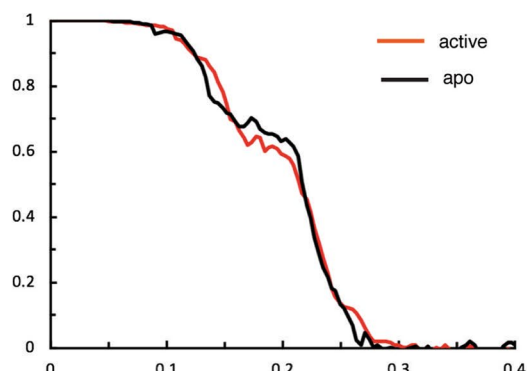
L-quisqualate and Nb43 in GDN (**c**). **d, e**, Cryo-EM class averages of inactive (**d**) and active mGlu5 bound to L-quisqualate and Nb43 (**e**). **f**, Particle angular distribution of the final cryo-EM reconstructions of apo (left) and active (right) mGlu5.



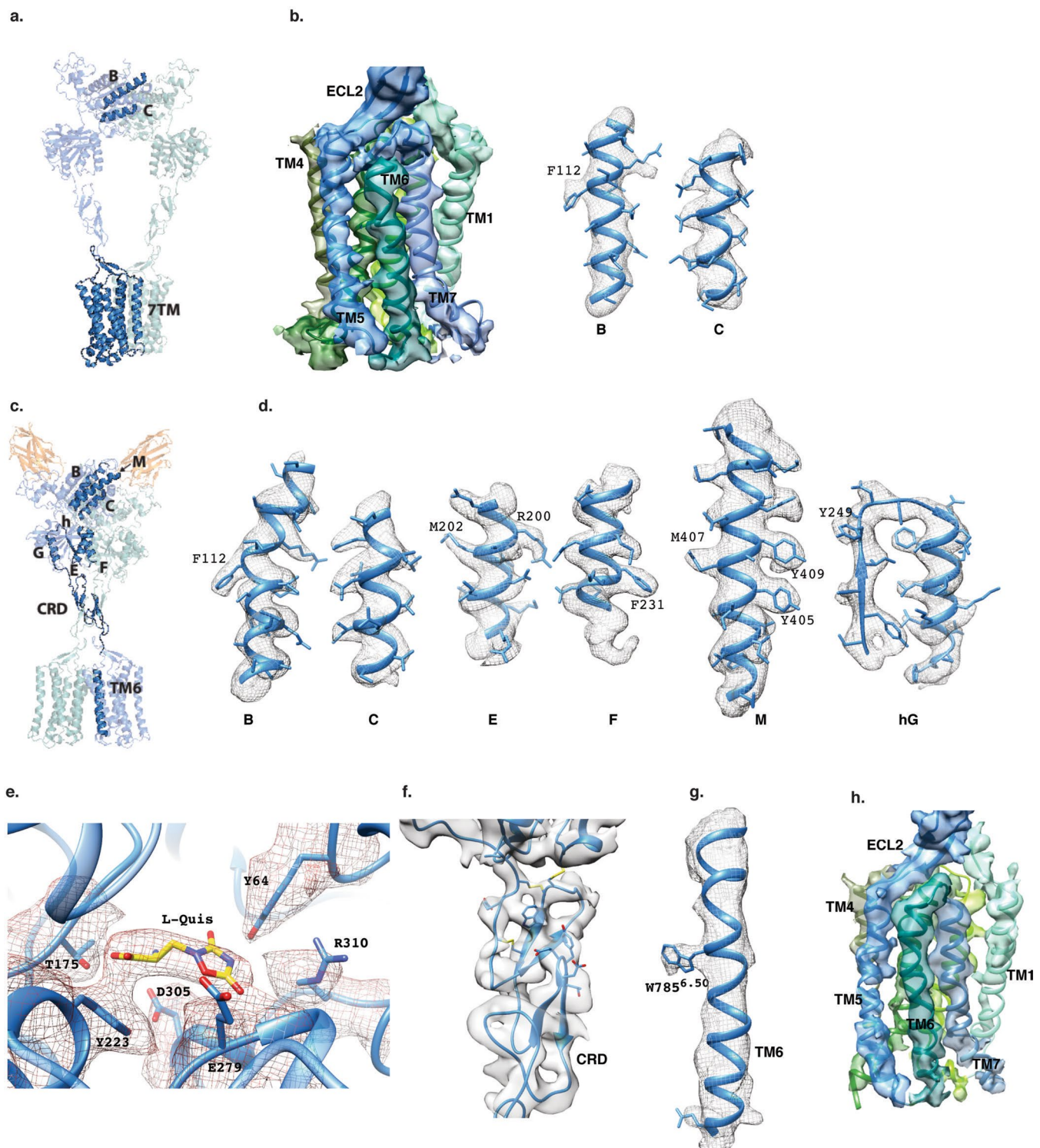
**Extended Data Fig. 3 | Cryo-EM 3D reconstruction workflow.** **a, b,** Processing workflow of apo mGlu5 in MSP1D1 nanodiscs (**a**) and apo mGlu5 bound to Nb43 in GDN (**b**).

**a.****b.**

**Extended Data Fig. 4 | Cryo-EM active-state processing and map resolution calculations.** **a.**, Flow chart indicating the processing of cryo-EM data for mGlu5 in complex with Nb43 and L-quisqualate. **b.**, Three-dimensional density maps of mGlu5 (left) and mGlu5 in complex

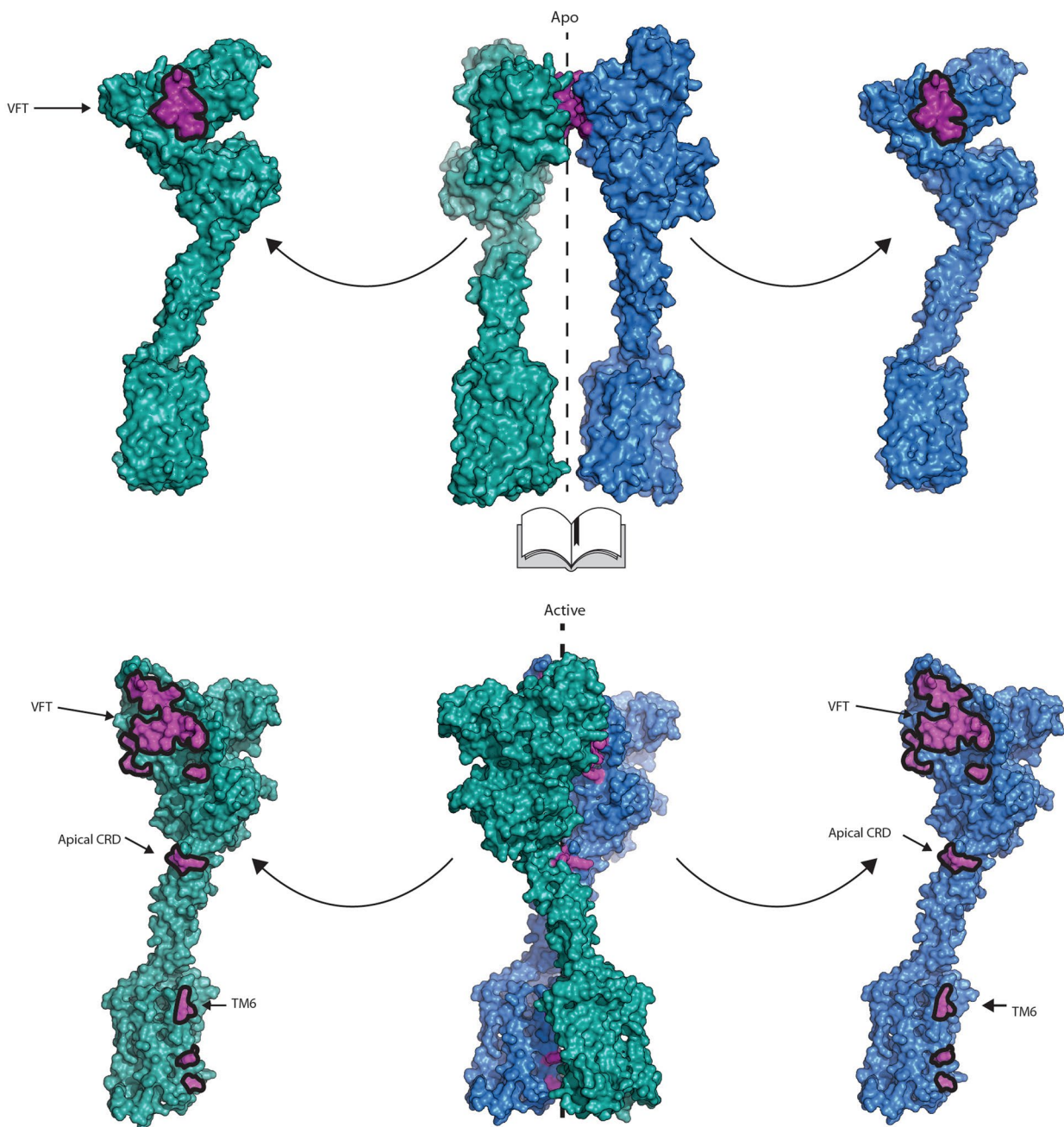
**c.**

with Nb43 and L-quisqualate (right), coloured by local resolution. **c.**, 'Gold standard' FSC curves from RELION indicate that the maps for both mGlu5 and mGlu5 in complex with Nb43 and L-quisqualate reach nominal resolutions of 4.0 Å at FSC = 0.143.



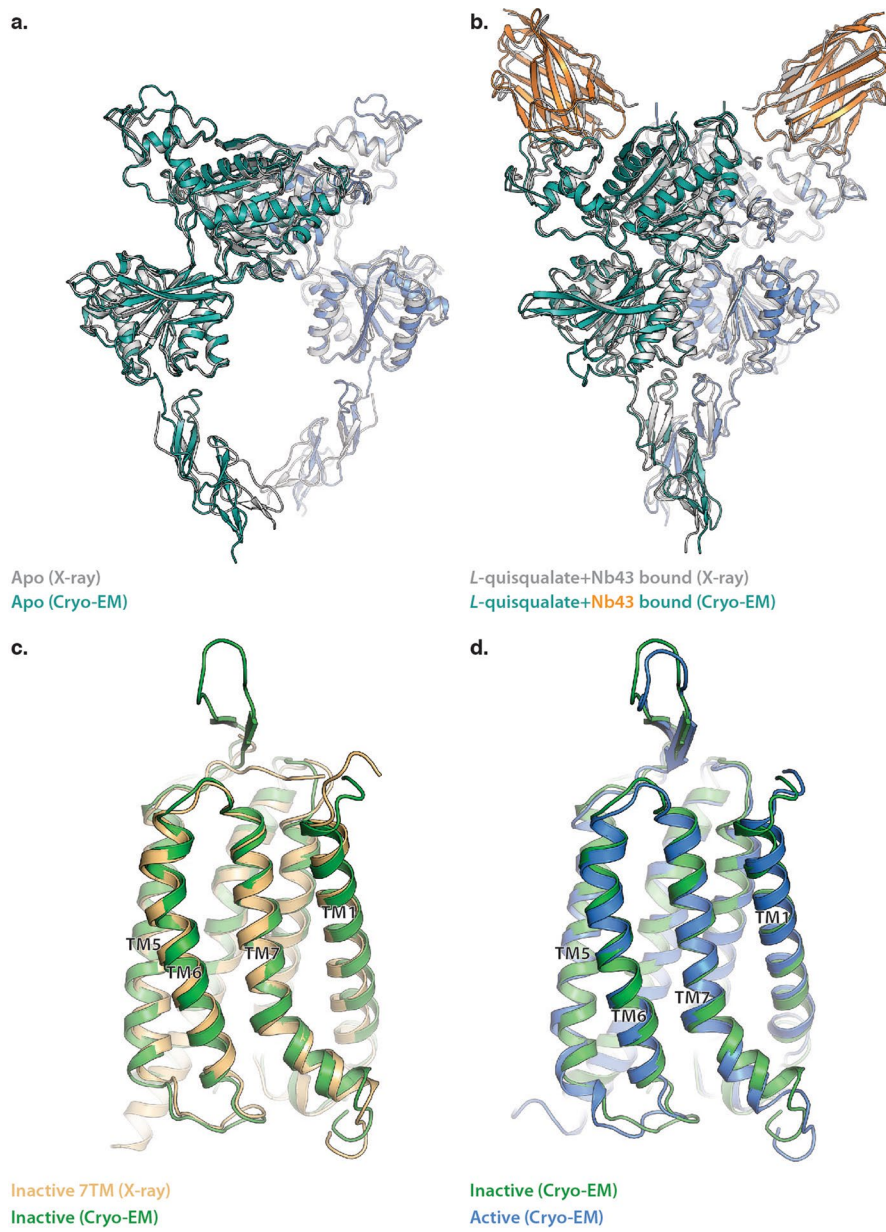
**Extended Data Fig. 5 | Agreement between the cryo-EM map and the model.** **a–h,** Representative cryo-EM densities and fitted atomic models for apo (**a, b**) and active (**c–h**) mGlu5. The B and C helices of the VFT and the 7TM domain are highlighted in **a** for the apo mGlu5 structure, and

density and model fits are shown in **b**. Various helices of the VFT, as well as the ligand-binding pocket, CRD and TM6 are highlighted in **c**, and their cryo-EM density and fitted models are shown in **d–h** for active mGlu5 bound to Nb43 and L-quisqualate.



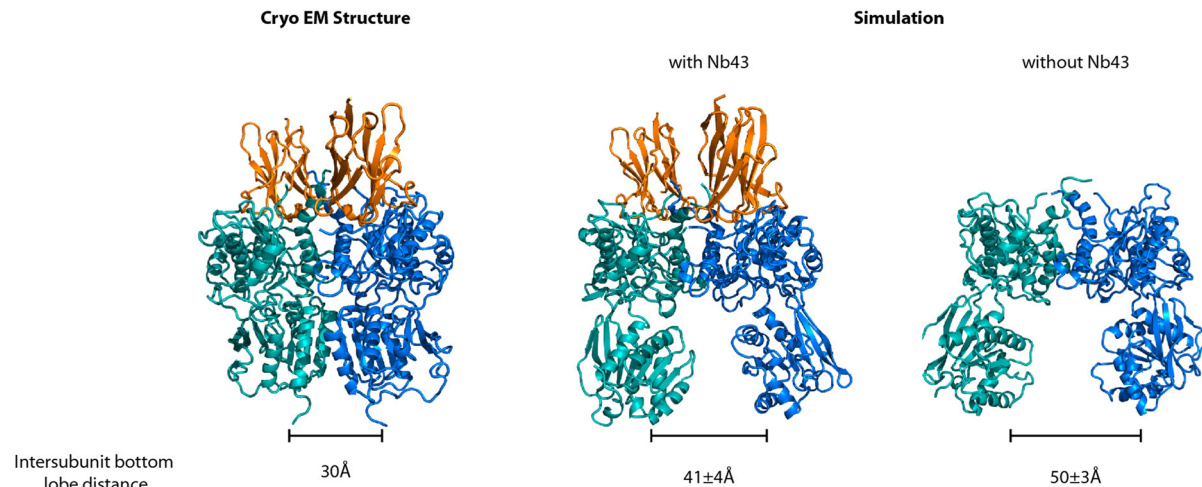
**Extended Data Fig. 6 | Comparison of the intersubunit interfaces in apo and active mGlu5.** Comparison of intersubunit interfaces in apo and active mGlu5 are shown for apo (top) and active (bottom) mGlu5. Contact

regions (purple) show residues within 4 Å of the opposite subunit. Notably, apo mGlu5 lacks any interactions beyond the VFT.



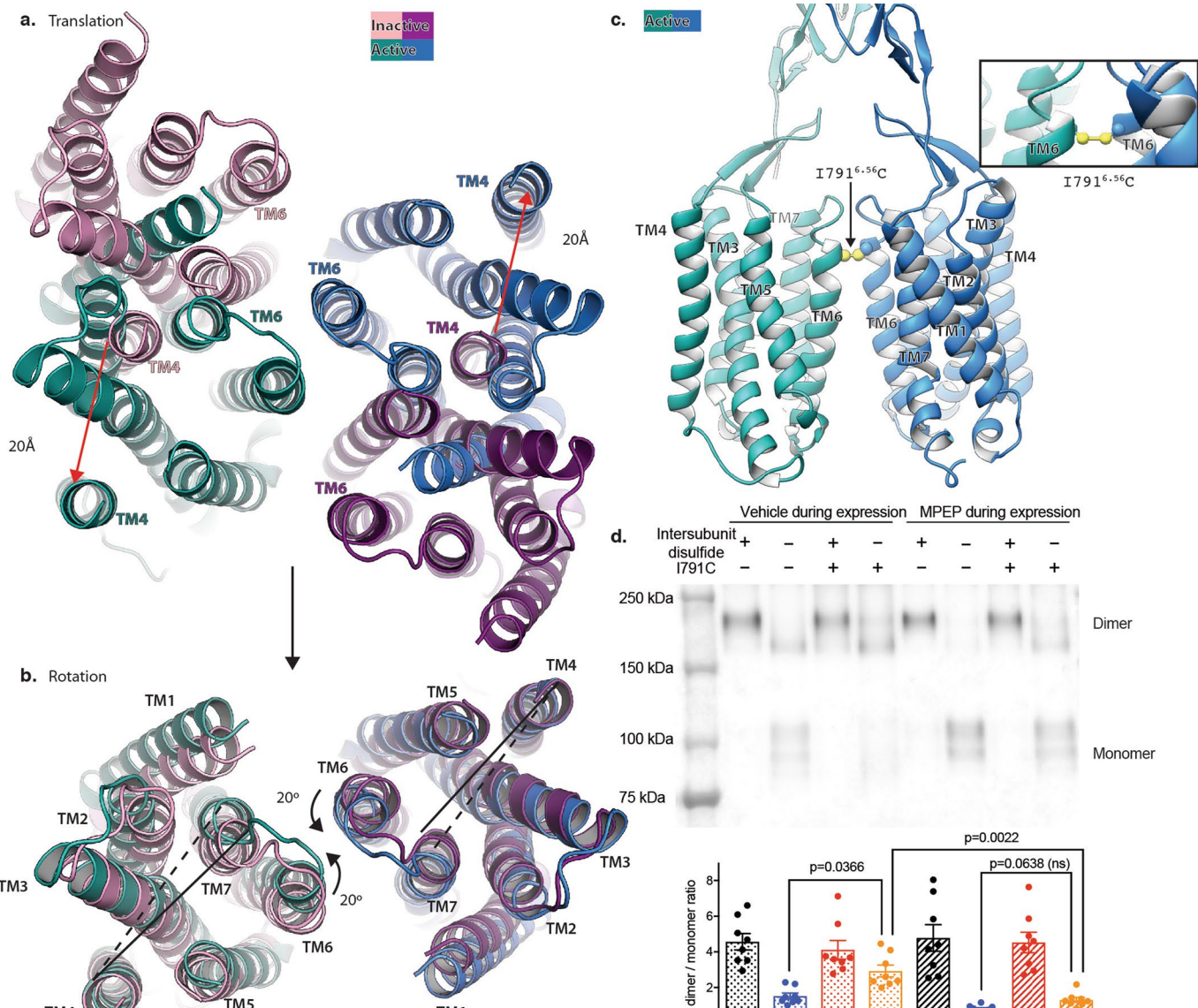
**Extended Data Fig. 7 | Comparison of cryo-EM structures of full-length mGlu5 with crystal structures.** **a**, The conformation of the VFT and CRD portions of full-length apo mGlu5 obtained using cryo-EM (coloured cartoon) is almost identical to the conformation revealed by the crystal structure of the full-length apo mGlu5 (7TM domain not resolved; grey cartoon). **b**, Similarly to the apo-state structures, the conformation of the VFT and CRD portions of full-length Nb43-bound, active-state

mGlu5 obtained by cryo-EM (coloured cartoon) is almost identical to the conformation revealed by the crystal structure of the ECD bound to *L*-quisqualate and Nb43. **c, d**, Despite being bound to a NAM (green) and a PAM (blue), the 7TM domains of in our full-length structures both align almost identically to a crystal structure of a NAM-bound 7TM domain in isolation (**c**) as well as to each other (**d**).



**Extended Data Fig. 8 | Molecular dynamics simulations of mGlu5 ECD-Nb43.** Simulation of the apo form of mGlu5 ECD both with and without Nb43. In the absence of Nb43, the ECD relaxes to an open conformation (right) with considerable separation between the bottom

lobes of the VFT. The presence of Nb43 restricts opening of the ECD to an intermediate degree (middle) but does not stabilize the compact resting state (left).



**Extended Data Fig. 9 | Structural transitions in the 7TM domain upon activation.** **a, b,** Activation involves a 20 Å translation of the 7TM domains relative to each other (**a**) followed by a 20° rotation around TM4 (**b**). The 7TM domains of the apo state are shown as shades of purple, whereas the active state 7TM domains are shown as shades of blue and teal. **c,** Model of the I791<sup>6,56</sup>C mutation on the active-state structure shows its ideal positioning for disulfide formation. **d,** Western blot analysis of

disulfide formation involving I791<sup>6,56</sup>C in both wild type and the C129A background in the presence and absence of the NAM MPEP. Bars in **d** (bottom) represent mean  $\pm$  s.e.m. from 8 independent experiments. Statistics were performed using repeated measures one-way ANOVA followed by Tukey's multiple comparisons test and indicated *P* values were adjusted to account for multiple comparisons.

## Extended Data Table 1 | Cryo EM and X-ray data collection and refinement statistics

## Cryo-EM data collection, refinement and validation statistics

	mGlu5 + MTEP (PDB 6N52) (EMDB 0346)	mGlu5 + C12PPB+L- quinalate+Nb43 (PDB 6N51) (EMDB 0345)	mGlu5 + Nb43 (EMDB 0347)
<b>Data collection and processing</b>			
Magnification	47,169	47,169	58,139
Voltage (kV)	300	300	300
Electron exposure (e <sup>-</sup> /Å <sup>2</sup> )	50	50	50
Defocus range (μm)	1.2–2.5	1.2–2.5	1.2–2.5
Pixel size (Å)	1.06	1.06	0.86
Symmetry imposed	C2	C2	C2
Initial particle images (no.)	1,696,744	2,490,831	694,742
Final particle images (no.)	123,096	73,472	44,831
Map resolution (Å)	4.0 Å FSC threshold (0.143)	4.0 Å (0.143)	7.9 Å (0.143)
Map resolution range (Å)	3.5–6	3.5–6	N/A
<b>Refinement</b>			
Initial model used (PDB code)	1EWK 4OO9	3LMK 4OO9	
Model resolution (Å)	4	4	
Model resolution range (Å)	4.8	3.5–7	
Map sharpening <i>B</i> factor (Å <sup>2</sup> )	-150	-150	
Model composition			
Non-hydrogen atoms	11206	13365	
Protein residues	1638 Residues (11150 atoms)	1876 residues (13283 atoms)	
Ligands	4 (51 atoms)	6 (82 atoms)	
R.m.s. deviations			
Bond lengths (Å)	0.004	0.006	
Bond angles (°)	0.757	0.845	
Validation			
MolProbity score	1.59	1.74	
Clashscore	4.74	5.59	
Poor rotamers (%)	0	0	
Ramachandran plot			
Favored (%)	94.97	93.23	
Allowed (%)	5.03	6.77	
Disallowed (%)	0	0	
EMRinger score	1.30	1.96	

## X Ray Data collection and refinement statistics

	mGlu5 ECD + Nb43 (PDB 6N4Y)	mGlu5 ECD + Nb43 and L-quinalate (PDB 6N50)	Fl. mGlu5 + FFMTEB (ECD-only model) (PDB 6N4X)
<b>Data collection</b>			
Space group	P 1 2, 1	P 1 2, 1	P 2 2 2,
Cell dimensions:			
a, b, c (Å)	95.53 158.4 112.0	150.4 157.2 208.1	119.08 174.1 189.9
α, β, γ (°)	90 101.93 90	90 90 90	90 90 90
Resolution (Å)	38.65–3.26 (3.38–3.26)*	39.29–3.75 (3.89–3.75)*	49.15–4.0 (4.14–4.0) *
<i>R</i> <sub>work</sub> or <i>R</i> <sub>free</sub>	0.076(0.49)	0.071 (0.61)	0.046(0.62)
<i>I</i> / <i>σI</i>	7.64(1.46)	9.86 (1.28)	11.55 (1.62)
Completeness (%)	98.2(94.3)	98.1 (96.7)	93.3(92.9)
Redundancy	2.0(1.9)	2.0 (1.9)	1.9 (1.9)
CC 1/2	0.93 (0.68)	0.931 (0.70)	0.999 (0.497)
<b>Refinement</b>			
Resolution (Å)	3.26	3.75	4.0
No. reflections	49354 (1999)**	25151 (1996)**	30267 (1538)**
<i>R</i> <sub>work</sub> / <i>R</i> <sub>free</sub>	0.199/0.250	0.270/0.304	0.256/0.276
No. atoms	19622	12178	7734
Protein	19317	12069	7649
Ligand/ion	205	109	85
Water	0	0	0
B-factors			
Protein	79.9	153.5	188.6
Ligand/ion	126.6	177.4	188.2
Water	N/A	N/A	N/A
R.m.s. deviations			
Bond lengths (Å)	0.004	0.003	0.002
Bond angles (°)	0.83	0.65	0.65

\*Values in parentheses are for highest-resolution shell.

\*\*Value in parentheses indicates *R*<sub>free</sub> set.

## Reporting Summary

Nature Research wishes to improve the reproducibility of the work that we publish. This form provides structure for consistency and transparency in reporting. For further information on Nature Research policies, see [Authors & Referees](#) and the [Editorial Policy Checklist](#).

### Statistical parameters

When statistical analyses are reported, confirm that the following items are present in the relevant location (e.g. figure legend, table legend, main text, or Methods section).

n/a Confirmed

- The exact sample size ( $n$ ) for each experimental group/condition, given as a discrete number and unit of measurement
- An indication of whether measurements were taken from distinct samples or whether the same sample was measured repeatedly
- The statistical test(s) used AND whether they are one- or two-sided  
*Only common tests should be described solely by name; describe more complex techniques in the Methods section.*
- A description of all covariates tested
- A description of any assumptions or corrections, such as tests of normality and adjustment for multiple comparisons
- A full description of the statistics including central tendency (e.g. means) or other basic estimates (e.g. regression coefficient) AND variation (e.g. standard deviation) or associated estimates of uncertainty (e.g. confidence intervals)
- For null hypothesis testing, the test statistic (e.g.  $F$ ,  $t$ ,  $r$ ) with confidence intervals, effect sizes, degrees of freedom and  $P$  value noted  
*Give P values as exact values whenever suitable.*
- For Bayesian analysis, information on the choice of priors and Markov chain Monte Carlo settings
- For hierarchical and complex designs, identification of the appropriate level for tests and full reporting of outcomes
- Estimates of effect sizes (e.g. Cohen's  $d$ , Pearson's  $r$ ), indicating how they were calculated
- Clearly defined error bars  
*State explicitly what error bars represent (e.g. SD, SE, CI)*

*Our web collection on [statistics for biologists](#) may be useful.*

### Software and code

Policy information about [availability of computer code](#)

Data collection

CryoEM Data was collected automatically on a Titan Krios (FEI) using SerialEM.  
Crystallography Data was collected using the Blu-Ice interface.  
Flow Cytometry Data was collected using a MoFlo Astrios cell sorter (Beckman Coulter) running Summit v6.2.

Data analysis

The following software was used in this study: MotionCor2, gCTF v1.06, RELION 2.1, CryoSparc v1, BSoft, UCSF Chimera 1.12.0, UCSF ChimeraX 0.7.0, Coot 0.8.8, PyMOL 2.1, Phenix v 1.14-3211, Rosetta v 2017.39.59729, OPLS-M/AA, VIPER, NAMD 2.12, VMD 1.9.3, Graphpad Prism v7, Maestro, Imager Lab 6.0, Swiss Model (webserver: <https://swissmodel.expasy.org>), XDS (version Jan 26, 2018), BUSTER (Global Phasing - version 20180515), PHASER as implemented in Phenix v 1.14-3211, RefMac as implemented in CCP4 v7.0.055, MolProbity as implemented in Phenix v 1.14-3211.

For manuscripts utilizing custom algorithms or software that are central to the research but not yet described in published literature, software must be made available to editors/reviewers upon request. We strongly encourage code deposition in a community repository (e.g. GitHub). See the Nature Research [guidelines for submitting code & software](#) for further information.

## Data

Policy information about [availability of data](#)

All manuscripts must include a [data availability statement](#). This statement should provide the following information, where applicable:

- Accession codes, unique identifiers, or web links for publicly available datasets
- A list of figures that have associated raw data
- A description of any restrictions on data availability

All data generated or analyzed during this study are included in this published article and its Supplementary Information. The X-ray crystal structures and structure factors of the apo mGlu5 ECD, of the apo-mGlu5 ECD with Nb43, and of the mGlu5 ECD bound to Nb43 and L-quisqualate have been deposited in the Protein Data Bank under accession codes 6N4X, 6N4Y, and 6N50 respectively. Cryo-EM Maps of apo mGlu5 in nanodiscs, apo mGlu5 bound to Nb43 and active mGlu5 bound to Nb43 and L-quisqualate in GDN have been deposited in the Electron Microscopy Data Bank under accession codes 0346, 0347, and 0345 respectively. The atomic coordinates of apo mGlu5 and active mGlu5 bound to Nb43 and L-quisqualate have been deposited in the Protein Data Bank under accession codes 6N52 and 6N51 respectively.

## Field-specific reporting

Please select the best fit for your research. If you are not sure, read the appropriate sections before making your selection.

Life sciences       Behavioural & social sciences       Ecological, evolutionary & environmental sciences

For a reference copy of the document with all sections, see [nature.com/authors/policies/ReportingSummary-flat.pdf](https://nature.com/authors/policies/ReportingSummary-flat.pdf)

## Life sciences study design

All studies must disclose on these points even when the disclosure is negative.

Sample size	Sample sizes were not predetermined by statistical methods. For cryo-EM and crystallography data, sample sizes were determined by availability of microscope and X-ray synchrotron beam time, respectively. Crystallography data was sufficient to obtain >90% completeness at the highest resolution. Cryo-EM data was collected until we were able to refine a high-resolution structure that allowed us to obtain a high-resolution reconstruction within the confines of limited microscope time. For signaling, we followed the standard practices in the field. In general, this consists of at least 3 independent experiments performed in triplicate. We believe this to be sufficient, and our estimates of the mean and SEM did not deviate by incorporating more experiments.
Data exclusions	No data was systematically excluded. The process of generating 3D maps from cryo-EM particles involves sorting for particles that are damaged, have low signal, or are in minority conformations that are unlikely to refine correctly. This is implemented in Relion 2.1 and cryoSparc and is standard in the field. There was, however, no pre-determined criteria for exclusion of particles.
Replication	All attempts at replication succeeded. In general, our data shows mean +/- SEM from 3-6 independent experiments (biological replicates, n) performed in duplicate or triplicate (technical replicates of the biological replicates). Figure 1b shows individual data points from a representative experiment (of 3 independent experiments in triplicate). The western blotting data shows lanes from at least 3 independent transfections. There was no attempt to replicate cryo-EM data. This data involves averaging of tens of thousands of particles.
Randomization	Randomization was not attempted nor necessary for this study. This was not a clinical trial or animal study that is dependent on randomization. All variables could be controlled.
Blinding	Blinding was not attempted or needed. There was no group allocation performed in this study.

## Reporting for specific materials, systems and methods

### Materials & experimental systems

n/a	Involved in the study
<input type="checkbox"/>	<input checked="" type="checkbox"/> Unique biological materials
<input type="checkbox"/>	<input checked="" type="checkbox"/> Antibodies
<input type="checkbox"/>	<input checked="" type="checkbox"/> Eukaryotic cell lines
<input checked="" type="checkbox"/>	<input type="checkbox"/> Palaeontology
<input type="checkbox"/>	<input checked="" type="checkbox"/> Animals and other organisms
<input checked="" type="checkbox"/>	<input type="checkbox"/> Human research participants

### Methods

n/a	Involved in the study
<input checked="" type="checkbox"/>	<input type="checkbox"/> ChIP-seq
<input checked="" type="checkbox"/>	<input type="checkbox"/> Flow cytometry
<input checked="" type="checkbox"/>	<input type="checkbox"/> MRI-based neuroimaging

## Unique biological materials

Policy information about [availability of materials](#)

### Obtaining unique materials

Nb43 is a unique biological material that was generated for the purpose of this study. Nb43 can be obtained upon request from Brian Kobilka (kobilka@stanford.edu)

## Antibodies

### Antibodies used

Anti-FLAG M2 (Sigma cat F3165), HRP-conjugated anti-mouse antibody (Thermo Scientific cat 32430), RPE-Conjugated FLAG antibody (Prozyme cat PJ315). We also used Nb43.

### Validation

Antibodies are validated by the manufacturers. Specifically, Anti-FLAG M2 is validated to detect 2 ng of FLAG-BAP fusion protein by dot blot using chemiluminescent detection (SIGMA). HRP conjugated anti-mouse antibody was validated by western blotting. RPE-Conjugated FLAG antibody (Prozyme) was validated by western blotting and subsequent detection. Nb43 validation is described in Figure 1 for its effects on potentiating orthosteric and allosteric ligands to mGlu5. Binding was verified both by SDS-PAGE (not shown) as well as the structures of Nb43 bound to mGlu5 ECD (by X-ray crystallography) as well as bound to full-length mGlu5 (cryo-EM). This shows direct binding and reveals the mode of binding.

## Eukaryotic cell lines

Policy information about [cell lines](#)

### Cell line source(s)

Sf9, Expression Systems, Cat 94-001S.  
Tni Cells (Hi-5), Expression Systems, Cat 94011S.  
HEK293 Cells (ATCC CRL 1573)

### Authentication

Cell lines are maintained by the supplier. No additional authentication was performed by the authors of this study.

### Mycoplasma contamination

Cell lines are tested by manufacturer for contamination, but not were not further tested by the authors of this study.

### Commonly misidentified lines (See [ICLAC](#) register)

No commonly misidentified lines were used in this study.

## Animals and other organisms

Policy information about [studies involving animals; ARRIVE guidelines](#) recommended for reporting animal research

### Laboratory animals

One adult Llama (Llama glama) was immunized with recombinant mGlu5. After immune response was deemed sufficient, blood was drawn from the llama to isolate B-cells that generate antibodies to mGlu5.

### Wild animals

No wild animals were involved in the study.

### Field-collected samples

No field-collected samples were used in this study.